

MECHANICAL PERFORMANCE, STRUCTURE AND FRACTOGRAPHY OF ABS MANUFACTURED BY THE FUSED FILAMENT FABRICATION ADDITIVE MANUFACTURING

A. Stern^{1,2}, Y. Rosenthal², D. Richkov¹,
O. Gewelber¹, D. Ashkenazi^{3,*}

¹School of Mechanical Engineering, Afeka Academic College of Engineering, Tel Aviv, 69107, Israel

²Department of Materials Engineering, Ben-Gurion University of the Negev, Beer Sheva 8410501, Israel

³School of Mechanical Engineering, Tel Aviv University, Ramat Aviv 6997801, Israel

*Corresponding author's e-mail address: dana@eng.tau.ac.il

ABSTRACT

Fused filament fabrication (FFF) is the most widely used additive manufacturing (AM) technology for printing thermoplastic materials, among them the ABS. A significant problem of 3D-printed parts manufactured by AM-FFF is the anisotropy of their mechanical properties. Thus, it is of great importance to understand the impact of the build strategy of the mechanical properties and failure mechanisms of AM-FFF ABS components. This research aims, at least partly, to fill this gap by studying the structure and mechanical behavior by performing fracture surface analysis of AM-FFF ABS specimens under the three-point bend test. For this purpose, three build orientations (flat, on-edge and upright), each built at 0°/90° and -45°/+45° raster angles and oblique printed samples (0°, 15°, 30°, 45°, 60°, and 75°) built at -45°/+45° raster angles were prepared. The results revealed that the build direction with the lowest density, the flexural modulus of elasticity, flexural strength, and deflection was in the upright direction for both 0°/90° and -45°/+45° raster orientations. Overall, two main failure modes were observed for the tested specimens: (1) inter-layer/inter-raster bond failure, which is the main contributor to failure of all upright samples and (2) intra-layer/trans-raster failure, which is the main contributor to failure of flat and on-edge specimens printed at -45°/+45° raster orientation. The results of the oblique printed samples demonstrate that a single crack initiation can transform into a few inter-laminar and intra-laminar fracture surfaces due to competing stress fields and structural gradients.

KEYWORDS: ABS polymer, additive manufacturing, fused filament fabrication, mechanical properties, three-point bend test, fractography and structure visualization

1. INTRODUCTION

Fused filament fabrication (FFF) is a commonly used additive manufacturing (AM) process, based on extrusion and mainly applied in rapid prototyping [1] – [11]. With the development of advanced materials and technology, the AM-FFF technique is shifting from manufacturing prototypes to the production of industrial end products. Mechanical properties need to be studied in detail to further bring the FFF technique into volume production in order to fabricate functional parts for new applications in many sectors of biomedical engineering, aerospace, civil engineering, and robotics [1] – [10]. For example, in the automotive industry, the AM-FFF method is used to print fixtures and jigs as well as prototypes for testing [2].

Many researchers have studied the mechanical behavior of AM-FFF components [1] – [9], [12] –

[17]. In general, parts manufactured using the AM-FFF process typically exhibit lower moduli, strength, and stiffness when compared to parts of the same geometry, fabricated from bulk polymers by conventional techniques [8]. The mechanical properties of AM-FFF parts depend on the product's geometric details, process parameters and thermoplastic polymer material [8], [18]. Because AM-FFF products are built in layers, the resulting structure and properties are expected to be anisotropic. The most common discontinuities in the printed parts are inter- and intra-layer porosity and imperfect bond-lines [12] – [24]. The FFF method is limited to materials with a low melting temperature. Therefore, thermoplastic materials are usually used, such as amorphous acrylonitrile butadiene styrene (ABS), which is probably the most broadly used thermoplastic polymer [11], [25]. The production of AM-FFF thermoplastics is significantly challenging because of the limitations related to high temperature

polymers, including large thermal gradients, non-equilibrium cooling, presence of residual stresses, the need to overcome the high viscosity of such polymers, and the inability of the printers to reliably conserve the essential high processing temperatures [25], [26].

The common ABS microstructure is composed of a continuous and stiff acrylonitrile-styrene phase with compatible polybutadiene inclusions, which results in a polymer that is both relatively tough and strong. This type of microstructure leads to complex failures, such as void coalescence, cavitation, localized shear yielding, and crazing [21]. Throughout the AM-FFF process, the ABS filament is deposited to generate for each layer a preset-specific build strategy. A permanent bonding of two neighboring layers is formed by the local thermal diffusion of adjacent rasters. The ABS raster in one-layer bonds with the rasters in the layer beneath it and solidifies [20]. This bonding takes place between neighboring rasters in the same layer (intra-layer) and among the sequential layers (inter-layer) [3], [4], where the bond creation includes surface contact between two rasters, neck growth and molecular diffusion at the interface between the layers [17], [20]. The common discontinuities in the printed layer are porosity located between the contour beads and the deposited rasters, porosity located between the deposited rasters, and poor bonding between rasters inside and in between the layers [8], [12], [15], [16], [20], [21].

The mechanical properties and structural integrity of AM-FFF parts are highly affected by the quality of the bonding [17], [20]. When an ABS part is produced by the AM-FFF technique, the process parameters, such as the raster angle, raster width, raster gap, infill density, extruder temperature, deposition speed, contour width, layer thickness and width, airgaps, and specimen orientation, play a significant role in providing improved strength to the 3D-printed object [2], [4], [6], [8], [27] – [29]. Other parameters, including filament quality and environmental issues, such as humidity and oxygen content, also affect the mechanical properties and the quality of the part [4], [30]. The temperature gradient between neighboring layers through solidification causes residual stresses, shrinkage, and distortion of the 3D-printed part [3]. Due to the formation of voids, the strength of the AM-FFF printed structure is lower than the strength of objects produced by other methods, such as injection molding [3], [31]. The quantity of voids within the AM-FFF ABS structure can be reduced by printing a smaller layer thickness, in order to improve the bond between layers, which decreases the inter-layer distortion that generates microvoids [2], [6], [8].

In the literature, many studies exist that use diverse specimen geometries with various printing directions and different raster orientations in order to examine the mechanical behavior of AM-FFF parts. For example, Cantrell et al. (2017) studied the tensile and shear properties of AM-FFF ABS specimens on

three different directions (flat, on-edge and upright) and four raster orientations ($0^\circ/90^\circ$, $+15^\circ/-75^\circ$, $+30^\circ/-60^\circ$, and $+45^\circ/-45^\circ$). Their results showed that, in the case of tensile specimens, the build direction and raster orientations have moderate effects on Young's modulus and Poisson's ratio. However, the shear modulus and shear offset yield strength vary by up to 33% between the different build directions and raster orientations [19]. The raster angle affects the anisotropy of AM-FFF parts and correspondingly impacts their mechanical behavior, including their strength [6]. For example, the elongation at break of 3D-printed PLA showed an anisotropic behavior with the largest and least values being of $+45^\circ/-45^\circ$ and $0/90^\circ$ raster angles, respectively [32]. The tensile strength of AM-FFF ABS specimens is mostly affected by the raster angle, raster width and layer height. This is because by changing the raster angle, the way the load is transferred within the specimens is also changed. When the raster angle rises, the bonding between neighboring filaments (intra-layer bond) is further involved in carrying the load. It has been widely publicized that the inter-layer raster-to-raster (layer-to-layer) bonding, shrinkage of the rasters, and higher porosity in particular orientations influence the properties of the printed parts and generate anisotropy [22] – [24], [27] – [29], [33] – [38]. In general, the reported tensile properties of AM-FFF polymers are lower than those of conventionally produced polymers, mostly because of voids existing in the AM-FFF specimens [4]. It has been observed by others that, for AM-FFF ABS tensile specimens, the $0^\circ/90^\circ$ raster orientation is similar to the crisscross ($-45^\circ/+45^\circ$) raster orientation in terms of tensile strength. However, the $-45^\circ/+45^\circ$ orientation provides increased flexural strength (FS) than the $0^\circ/90^\circ$ orientation. In addition, the impact strength value is higher for the $-45^\circ/+45^\circ$ orientation than for the $0^\circ/90^\circ$ orientation [6].

AM-FFF parts have so far proved to be insufficient for high-load concentration applications because their main type of failure is crack propagation that results from the delamination of layers [10]. Scanning electron microscope (SEM) observation of the fractured surface of AM-FFF thermoplastics has revealed the presence of voids, cracks and air gaps [13]. The strength of AM-FFF parts may be reduced when a crack is presented. Moreover, AM-FFF parts may experience different loading conditions that may lead to the failure of the structure according to crack propagation. The weakest point of parts produced by AM-FFF is the interface between adjacent laminae and deposition toolpaths or rasters, limiting the strength of the overall part [12]. Ayatollahi et al. (2020) found that the fracture load can vary up to 100% depending on the raster orientation. The $-45^\circ/+45^\circ$ specimens had the highest and the $0/90^\circ$ specimens had the least fracture resistance [32]. Fractographic analysis can provide important details concerning the fracture behavior and the cause of

fracture of AM-FFF samples [39]. Riddick et al. (2016) examined the tensile failure of AM-FFF ABS specimens by fractographic analysis. For that purpose, tensile specimens were 3D-printed on flat, on-edge and upright directions and 0° , 90° , $0^\circ/90^\circ$, and $-45^\circ/+45^\circ$ raster orientations. Their results showed anisotropy of the mechanical properties when exposed to axial tensile loading. Fractographic observation revealed that the specimens with on-edge build direction filled the voids more than the other directions [17]. Hart and Wetzel (2017) produced AM-FFF single-edge cracked ABS specimens with various layer orientations [36]. Their examination of the fracture surface following bending tests revealed ductile fractures (high energy) for the cross-laminar crack propagation and brittle fracture (low energy) for the inter-laminar crack propagation. Moreover, the inter-laminar fracture toughness was around one order of magnitude lower than the cross-laminar toughness [7], [36]. Garg and Bhattacharya (2017) examined AM-FFF tensile specimens and found that 0° raster layers show brittle fracture by tearing and rupture of single layers. Yet in 90° raster layers the failure occurred owing to separation of layers from the neighboring bonds (delamination) [16]. Verma et al. (2021) studied the fracture behavior of AM-FFF ABS by using tension specimens with double-edge-notch. Their SEM fractography observation revealed that crack propagation by ductile failure mechanisms involves void growth and coalescence, resulting in drawing and ductile tearing of the polymer [12]. Fatigue properties of AM polymers, including ABS, have been widely studied [39]. Ziemian et al. (2016) studied the behavior of AM-FFF ABS samples during cyclical fatigue loading. Their results showed that the fatigue behavior of AM-FFF polymers is similar to reinforced composites, causing a reduction of the effective Young's modulus. In addition, the observed main fatigue failure mechanisms were fiber cracking, delamination, crazing, and void geometry changes [40]. There is still uncertainty about how to evaluate fracture mechanics in AM-FFF polymers since conventional standards are frequently not appropriate for anisotropic and inhomogeneous AM parts [37]. For ABS parts subjected to a tensile load, crazing is a known failure mechanism [36], [38], [41]. In the AM-FFF ABS specimens, crazes appear below the yield strength, σ_y , after reaching a stress value of about $0.8 \sigma_y$. Following the yielding, the original craze spreads from the initiation sites across the entire specimen's cross-section; crazing in AM-FFF ABS is usually $100 \mu\text{m}$ thick [38].

Since the mechanical properties of AM-FFF ABS components are anisotropic, it is of great importance to understand the influence of the build strategy on the mechanical properties and failure mechanisms of such printed components. Most studies that exist in the literature, on the mechanical behavior of AM-FFF ABS, use tensile test methods and generally provide the Young's modulus, yield

strength, ultimate strength and elongation [4] – [6], [9], [17], [18], [27], [29], [35], [37], [42]; fewer works have examined the impact, flexural, fatigue, and compression properties of the 3D-printed ABS material [1], [4], [5], [21] – [25], [29]. The novelty of the current research is that it aims, at least partly, to fill this gap by studying the structure, mechanical behavior, and fracture surface of AM-FFF ABS specimens under the three-point bend test condition. In the present study, as a part of an ongoing project [1], [22] – [24], an effort has been made to gain further knowledge concerning the mechanical properties, structure, and fracture behavior of AM-FFF ABS specimens examined by three-point bend testing. The structure, including discontinuities in 3D-printed samples was visualized and analyzed. The evaluation of porosity may provide a method to achieve simple toughening for a range of AM-FFF materials including ABS [38]. A series of tests were conducted to determine the flexural properties in the three principal build orientations and to study the significance of the raster angles. Finally, the fractured samples were further examined via reflected and transmitted light microscopy to determine delamination behavior and fracture pathing.

2. EXPERIMENTS

2.1. Specimens

This paper describes the manufacturing method, experimental procedures, and outcomes from the characterization of the AM-FFF ABS specimens. This research focused on the characterization of the mechanical properties in bending (according to the ASTM D790 standard for three-point bending [43]) of ABS plus© (Table 1) [44], a common thermoplastic polymer, used for many purposes. The ASTM D790 standard is commonly used in order to determine the flexural properties of reinforced and unreinforced plastics, including 3D-printed thermoplastics [1], [2], [4], [6], [29], [33]. All ABS specimens were designed with a computer-aided design (CAD) program, using a SolidWorks program, and were built with a STRATASYS© Dimension Elite© FFF machine system. The dimensions of the designed specimens were $127 \text{ mm} \times 12.7 \text{ mm} \times 3.2 \text{ mm}$ (Fig. 1a).

Table 1. The ABS plus© general properties, as received from the Stratasys, Ltd. Manufacturer [44]

Properties	Typical value
Specific gravity	1.04 g/cm^3
Yield tensile strength	31 MPa
Ultimate tensile strength	33 MPa
Flexural strength	35 MPa
Tensile modulus	2,200 MPa
Flexural modulus	1,650 MPa
Tensile elongation at break	6 %

Properties	Typical value
Glass transition temperature (T _g)	108 °C
Coefficient of thermal expansion	8.82×10^{-5} mm/mm/°C

The specimens were produced with ABS plus[®] thermoplastic filament on three build orientations (flat, on-edge and upright) with 0°/90° and -45°/+45° raster orientation. In all specimens, each layer had a single outer raster line to define the layer's perimeter; each layer was composed of individual raster lines whose orientation varied between the layers according to the printing strategy (Fig. 1). The printing extrusion's measured temperature was 285 °C, the building chamber measured temperature was 70 °C, the layer thickness was 0.178 mm, and the nozzle speed during extrusion was up to 12.7 mm/sec, as recommended by the manufacturer [22], [24]. There are three available material filling options for this system (low density, high density and solid). The specimens of the present research were printed using the solid mode.

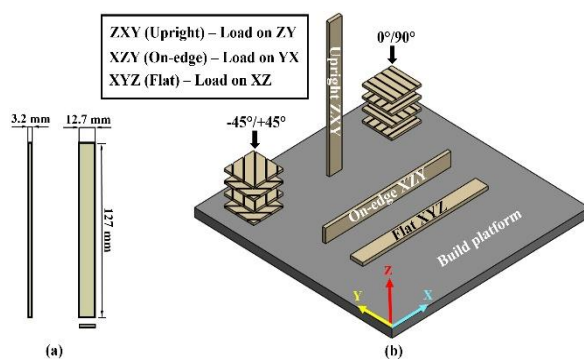


Fig. 1. The three-point bend test specimens: a) side, front and top views; b) an isometric Solidworks CAD model of the specimens, showing the six selected print strategy configurations: flat 0°/90°, flat -45°/+45°, on-edge 0°/90°, on-edge -45°/+45°, upright 0°/90° and upright -45°/+45° specimens. The directions of the bend loads on the specimens are shown in the square above

Standard beam-shaped three-point bending specimens in accordance with the ASTM D-790 standard [43] were additively manufactured in three main hatching strategies marked as upright, on-edge, and flat (ZXY, XZY, and YXZ, Fig. 1b), respectively, as termed by ISO/ASTM52921:2013 [45]. In this notation, orientations of the samples are identified by the three-letter label, established upon a specimen's bounding box being aligned parallel to the X, Y, and Z axes. The first lists the axis parallel to the longest dimension, followed by the axis parallel to the second longest dimension, and lastly, followed by the axis parallel to the shortest dimension [1]. As mentioned above, each group of the printed specimens includes two sub-groups, marked as 0°/90° and -45°/+45°,

resulting in a total of six groups of specimens covering all main printing orientations: flat 0°/90°, flat -45°/+45°, on-edge 0°/90°, on-edge -45°/+45°, upright 0°/90° and upright -45°/+45°. The filling modes (-45°/+45° and 0°/90°) were chosen to characterize the anisotropic behavior of AM-FFF ABS for the most commonly employed in-plane raster angles under the three-point bend test. Forty-two ABS specimens (five flat 0°/90°, five flat -45°/+45°, eleven on-edge 0°/90°, eleven on-edge -45°/+45°, five upright 0°/90° and five upright -45°/+45° configurations) were produced at six different printing strategies (Fig. 2a). To obtain the mechanical properties in 3D-orientation, an additional group of specimens was printed at different angles related to the print platform. Eighteen oblique specimens were successfully printed on separate trays at different building angles to the XY plane: 0°, 15°, 30°, 45°, 60° and 75°, three specimens for each angle (Fig. 2b). The 0° specimens are identical to the on-edge -45°/+45° configuration, however, they were 3D-printed on two separate trays. The upright 0°/90° specimens' configuration is identical to the 90°.

Dimension (Tables 2 and 3) and density (Table 4) were measured and calculated prior to the bending test. The l, h and b dimensions (Appendix A, Fig. A1) of the six configurations are shown in Table 2 and the dimensions for the oblique samples are shown in table 3. The height and width of the samples were measured by micrometer with an error of 0.01 mm; the length was measured by digital caliper with an error of 0.02 mm. The mass was weighted by analytical balance with an error of 0.0001 g. The volume of the specimens was divided by the mass in order to calculate the absolute density. Relative density was obtained by dividing the absolute density by the ABS supplier's provided density (Table 1).

2.2. Mechanical Testing

The three-point bend test involved collecting load-deflection data during the bend tests of specimens printed on the different orientations. The tests were conducted with a computerized MTS[®] Model E43-504 universal testing machine equipped with a three-point bend fixture and a deflection gage, using a crosshead velocity of 0.5 mm·min⁻¹. The positions and the bending load directions of the specimens were applied according to ASTM D-790 standard [43]. The test specimen beam of rectangular cross-section (12.7 mm × 3.2 mm) was supported by two anvils and the loading nose bent the beam by applying a load in the center, between the support anvils (Appendix A, Fig. A1). Load and axial deflection were acquired online during the test and used to calculate and obtain all the relevant mechanical parameters, e.g., load vs. deflection curves, the flexural modulus of elasticity (FME), and the FS. The applied load (initial load was 15 N) was measured in Newton with a 0.5% error and the axial deflection with an error of 0.02 mm.

Table 2. Dimensional accuracy of the as-printed three-point bend test specimens for the six print strategies (Fig. 1). l is the specimen's length, and b and h are the cross-section specimen's dimensions (Fig. 1a), for flat (F), on-edge (OE) and upright (UR) configurations

Dimension		Specimen configuration					
		F-45°/+45°	F0°/90°	OE-45°/+45°	OE0°/90°	UR-45°/+45°	UR0°/90°
l (mm)	Average	127.5±0.1	127.3±0.1	127.2±0.1	127.4±0.1	127.3±0.0	127.1±0.1
	Nominal	127.0	127.0	127.0	127.0	127.0	127.0
h (mm)	Average	12.8±0.0	12.7±0.0	12.7±0.1	12.8±0.1	12.8±0.1	12.8±0.0
	Nominal	12.7	12.7	12.7	12.7	12.7	12.7
b (mm)	Average	3.1±0.1	3.2±0.1	3.2±0.1	3.1±0.0	3.1±0.1	3.2±0.1
	Nominal	3.2	3.2	3.2	3.2	3.2	3.2

Table 3. Dimensional accuracy of the as-printed three-point bend test specimens printed at different angles (Fig. 2b)

Dimension		Specimen configuration					
		0°	15°	30°	45°	60°	75°
l (mm)	Average	127.5±0.0	127.5±0.0	127.4±0.0	127.2±0.0	127.2±0.0	127.3±0.0
	Nominal	127.0	127.0	127.0	127.0	127.0	127.0
h (mm)	Average	12.8±0.1	12.9±0.1	12.9±0.0	12.7±0.1	12.7±0.0	12.7±0.0
	Nominal	12.8	12.8	12.8	12.8	12.8	12.8
b (mm)	Average	3.2±0.0	3.2±0.0	3.2±0.0	3.3±0.0	3.2±0.0	3.2±0.0
	Nominal	3.2	3.2	3.2	3.2	3.2	3.2

Table 4. The relative density of the CAD model ρ_{CAD} (%) vs. the AM-FFF specimens' relative density ρ_{AM-FFF} (%), where F represents the flat configuration, OE represents the on-edge configuration and UR represents the upright configuration

Specimen configuration	ρ_{AM-FFF} (%)	ρ_{CAD} (%)
F0°/90°	95.4–95.7	92.6
F-45°/+45°	94.4–95.9	90.3
OE0°/90°	94.4–97.9	90.5
OE-45°/+45°	93.9–98.1	90.0
UR0°/90°	88.7–91.0	89.1
UR-45°/+45°	89.1–92.1	89.5

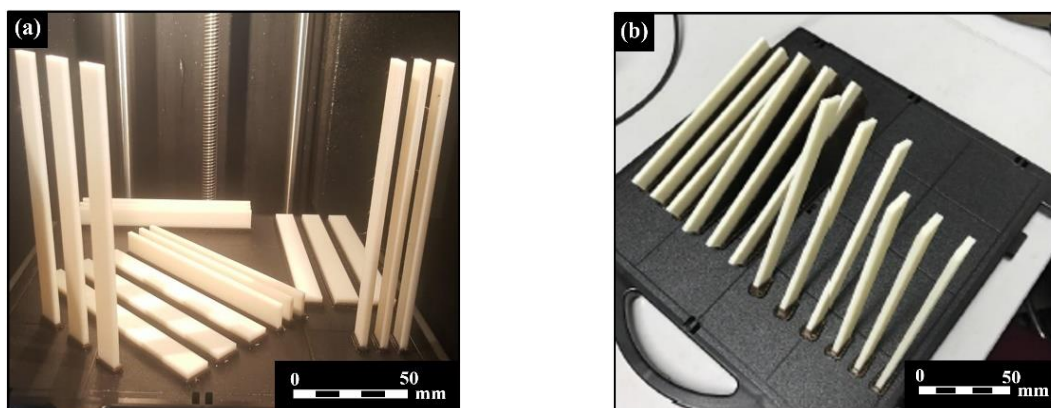


Fig. 2. The experimental AM-FFF ABS three-point bend test specimens, showing: a) the six selected print strategy configurations (flat 0°/90°, flat -45°/+45°, on-edge 0°/90°, on-edge -45°/+45°, upright 0°/90° and upright -45°/+45° specimens); b) the bend test specimens at different building angles (0°, 15°, 30°, 45°, 60° and 75°)

The flexural strength (MPa) of the three-point bend test specimens, σ_b , was calculated using the formula [46]: $\sigma_b = \frac{3FL}{2bh^2}$ where F is the maximum applied load (N) at the fracture point, L (mm) is the distance between the two anvils, b (mm) and h (mm) are the measured dimensions (width and thickness) of the specimen's cross-section (CS) (Appendix A, Fig. A1). The Stratasys data sheet for ABS material used in this study includes bending properties for two different build orientations [44].

2.3. Structure Visualization and Fractographic Methods

CAD visualization modeling of the AM-FFF specimen structure was performed with Autodesk Inventor 2021 software, based on the nominal dimensions of the printed specimen, and according to the following assumptions: (a) the layered rasters have an elliptical CS of 0.43 mm \times 0.18 mm, (b) the overlap (penetration) in the model simulates the welds between the adjacent rasters and the size of the overlap, determined by the size of the welds between rasters, (c) there is an overlap between the contour rasters and the adjacent infill rasters, (d) there is an overlap between the adjacent rasters of the same layer (intra-layer bonding), (e) there is an overlap between the rasters of the adjacent layers (inter-layer bonding), and (f) the specimens were printed in solid mode.

For flat and on-edge specimens, full-size 3D models were built on both orientations ($0^\circ/90^\circ$ and $-45^\circ/+45^\circ$). Due to technical constraints, the upright models in both orientations were partially built on the Z-axis direction. For the upright $0^\circ/90^\circ$ specimen, 40 layers were built on the Z-axis direction, and for the upright $-45^\circ/+45^\circ$ specimen, 250 layers were built on the Z-axis direction. During the modeling processes, an attempt was made to simulate the path line of a printing head in order to reach an infill level similar to that of the printed specimens.

To validate the modeling results, a relative density of the CAD models ρ_{CAD} % was calculated and compared to the measured relative density ρ_{AM-FFF} % of printed the specimens. The CAD model density ρ_{CAD} was calculated from the mass of the CAD model divided by the CAD model volume according to the dimensions of the specimen in the CAD model. The relative density of the CAD model, ρ_{CAD} %, was calculated from the CAD model density ρ_{CAD} divided by the density of ABS ($\rho_{ABS}=1.04 \text{ g/cm}^3$). The ρ_{CAD} in % vs. ρ_{AM-FFF} in % is presented in table 4.

Visual testing (VT) inspection combined with a multifocal digital light microscope (LM) and a confocal microscope observation were performed following the mechanical testing to observe the quality of the printed surfaces, including possible defects, as well as to examine the fracture surface morphology. The multifocal HIROX RH-2000 3D digital LM instrument is equipped with high-intensity LED lighting and an improved light sensitivity sensor

with a multi-focus system that contains powerful software. The Olympus LEXT OLS4100 confocal microscope is a laser scanning digital microscope equipped with a 405 nm laser for surface observation and measurements at 10 nm resolution. It consists of an optical system and high numerical apertures for non-contact 3D imaging and interpretations.

2.4. Delamination and Crack Propagation Measurements

Transmitted-light fractography (TLF) [24] was developed and adapted (Appendix A, Fig. A2) to examine and visualize the surface of the specimens and the in-depth phenomena in the surroundings of the crack path. The TLF system consists of an Olympus[®] BX43 biological computerized microscope equipped with an Olympus[®] DP-73 video camera, controlled by a cellSense Entry1.9 program (Olympus[®] Corporation, 2009-2013). Transmitted light (sometimes referred to as transillumination) shines light from a light illuminator through the specimen, to the viewing lens. It is used for transparent or translucent objects, commonly found in prepared biological specimens (e.g., slides) or with thin sections of opaque materials. This method may assist in determining whether the failure results from interlaminar crack propagation, cross laminar crack propagation, or mixed cross laminar and interlaminar crack propagation (Appendix A, Fig. A2) [3], [7], [36].

3. RESULTS

3.1. Dimensional Accuracy and Density

In order to analyze the dimensional accuracy of the current AM-FFF printing process, the dimensions of all 60 specimens were measured and the average values and the standard deviations were calculated (Tables 2 and 3). A satisfactory agreement was achieved between the dimensions of the 3D-printed specimens and the nominal CAD values for the six configurations (Table 2). A decent agreement was also achieved between the dimensions of the specimens printed at different angles and the nominal CAD values (Table 3).

The ρ_{CAD} % vs. the ρ_{AM-FFF} % for the six configurations is presented in Table 4. The ρ_{AM-FFF} % was between 88.7 % and 98.1 % (for the upright $0^\circ/90^\circ$ and on-edge $-45^\circ/+45^\circ$ configurations, respectively), whereas the ρ_{CAD} % was between 89.1 % and 92.6 % (for the upright $0^\circ/90^\circ$ and flat $0^\circ/90^\circ$ configurations, respectively) (Table 4).

3.2. Mechanical Properties

Deflection vs. load curves were obtained for the six configurations by performing three-point bend tests (Appendix A, Fig. A3 and Tables A1-A6).

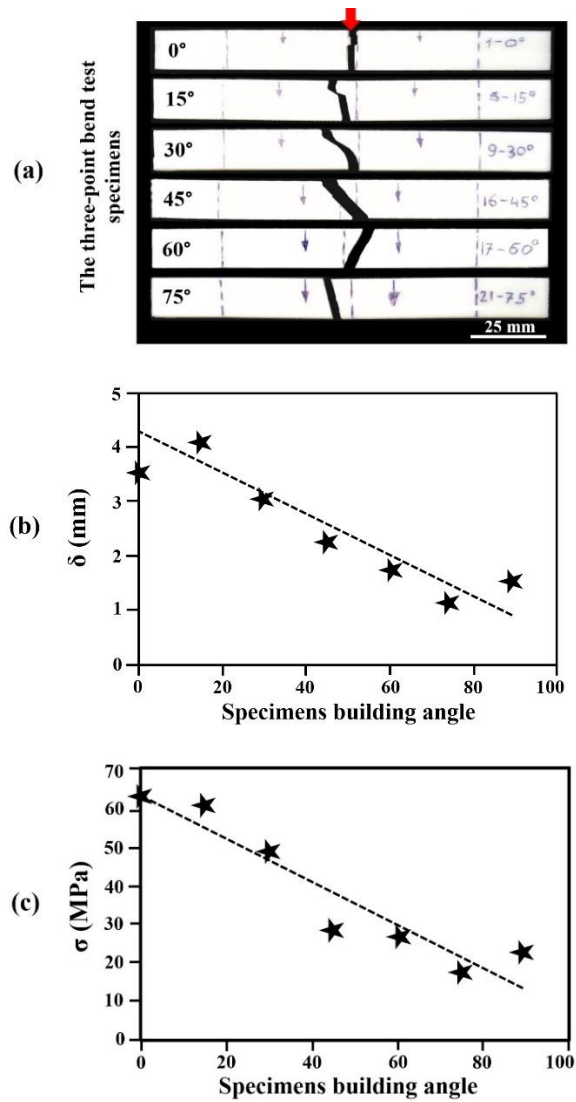


Fig. 3. View of the external surface of the ABS oblique specimens (see Fig. 2b) after they were fractured during the three-point bend test: a) 0°, 15°, 30°, 45°, 60°, and 75° building angles; b) deflection, δ , as function of specimens building angle; c) flexural strength, σ , as function of specimens building angle

Table 5. Properties of the six different configurations of the AM-FFF ABS three-point bending experimental results, where ρ_{AM-FFF} % is the AM-FFF specimens' average relative density, δ is the average deflection, σ is the average flexural strength and E_{FEM} is the average flexural modulus of elasticity, where F represents the flat configuration, OE represents the on-edge configuration and UR represents the upright configuration

Specimen configuration	ρ_{AM-FFF} (%)	δ (mm)	σ (MPa)	E_{FME} (MPa)
F0°/90°	95.5±1.0	3.2±0.2	58.3±1.5	1944±10.0
F-45°/+45°	95.3±1.0	5.4±0.3	62.8±1.3	1943±10.0
OE0°/90°	96.8±1.3	4.9±0.4	70.4±1.1	2141±11.0
OE-45°/+45°	96.3±1.9	5.0±1.3	65.4±1.8	2104±11.0
UR0°/90°	91.1±0.6	1.5±0.1	24.2±0.6	1419±8.0
UR-45°/+45°	91.1±1.0	1.4±0.1	24.8±2.5	1508±8.0

The average results of the 90° (upright) specimens shown in Fig. 3b-c were reported by Gewelber et al. (2020) [1]. The average mechanical properties of the six configurations of the AM-FFF ABS three-point bending experimental results are summarized in table 5. The calculated FME (E_{FME}) of all six configurations is also presented in table 5, where the upright 0°/90° and upright -45°/+45° filling modes have the lowest FME values.

The most noteworthy results are the properties of the samples printed in the vertical direction. The upright specimens exhibit the lowest toughness and FS, as the load is applied in this direction such that the rasters do not carry the load; instead, the bonds between adjacent layers (rasters) bear the tensile stresses. The data agree with the aforementioned observations that the layer-to-layer interface bonding is weaker than the overall mechanical properties of the bonded filaments located inside the layers.

Each examined oblique specimen (0°, 15°, 30°, 45°, 60°, and 75°, Fig. 3 and Table 6) exhibited a different pattern of crack propagation during the three-point bend test (Fig. 3a). The results indicated that the high-angle specimens had lower FS and deflection values than the low-angled bending specimens (Fig. 3b-c). The mechanical properties of the high-angle AM-FFF ABS specimens are mainly dictated by the bonding between the layers and are only slightly influenced by the rasters' orientation. Hence, the failure is of the inter-layer type.

Figure 4 illustrates FS and deflection at break vs. density (Fig. 4a-b), as well as the flexural strength vs. the deflection (Fig. 4c-d) for each build strategy. The on-edge samples have a slightly higher FS up to 70 MPa, while both flat -45°/+45° and on-edge samples have almost the same deflection at a break of about 5 mm (Fig. 4).

AM-FFF ABS specimens exhibit the expected strong anisotropic properties, displaying different mechanical properties when measured in different directions; the orientation with the lowest deflection (Fig. 4a) and the lowest FS (Fig. 4b) is in the upright configuration (Table 5).

Table 6. Properties of the tilted AM-FFF ABS specimens (Fig. 2b), where ρ_{AM-FFF} % is the AM-FFF specimens' average relative density, δ is the average deflection, σ is the average flexural strength. The 0° specimens' configuration is similar to the on-edge (OE) $-45^\circ/+45^\circ$ specimens

Specimen angle	ρ_{AM-FFF} (%)	δ (mm)	σ (MPa)
0° (similar to OE- $45^\circ/+45^\circ$)	94.8	3.5	63.2
15°	92.7	4.1	61.2
30°	91.8	3.0	49.1
45°	88.8	2.2	34.6
60°	88.1	1.7	26.4
75°	86.6	1.1	18.0

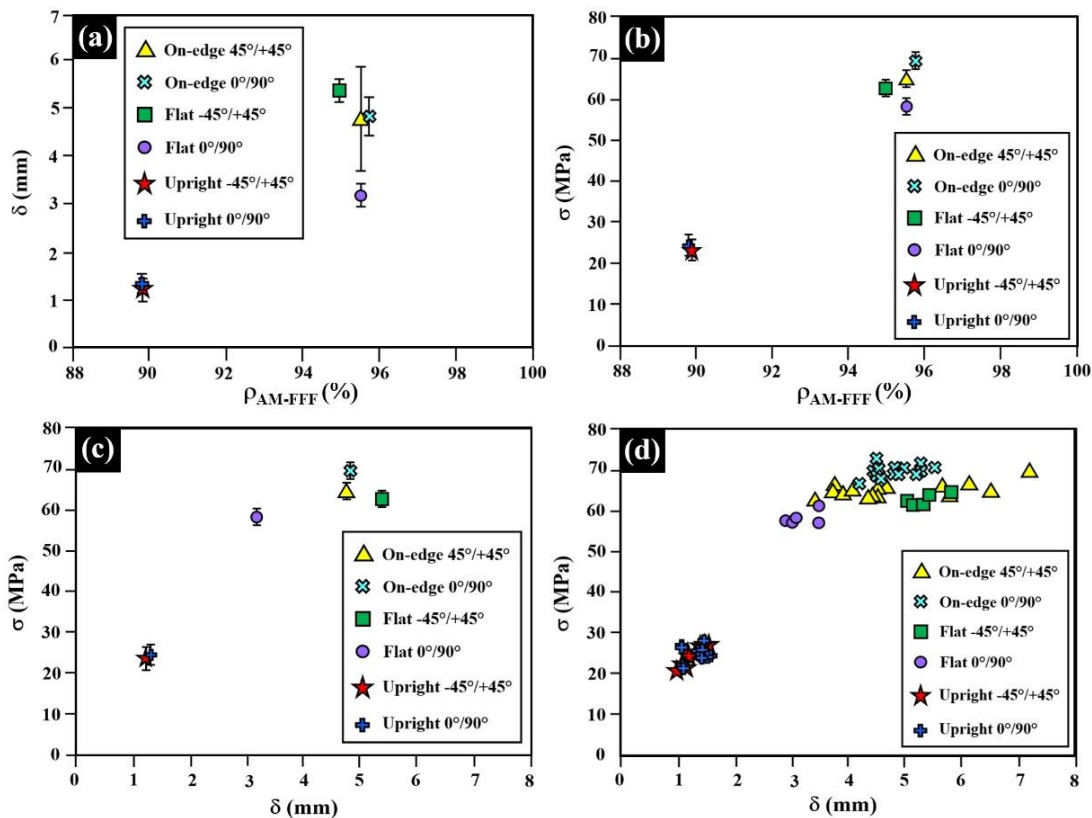


Fig. 4. AM-FFF ABS three-point bend test results of the on-edge, flat and upright configurations: a) average values of deflection, δ , vs. relative density, ρ_{AM-FFF} %, of printed specimens; b) average values of flexural strength, σ , vs. density; c) average values of flexural strength vs. average value of the deflection; d) flexural strength vs. the values of deflection for all the specimens

3.3. Fractography

During the three-point bend test, the upright specimens suddenly failed, without any warning, as expected for brittle fracture, whereas the flat and on-edge specimens failed after some plastic deformation, which indicates a relatively ductile fracture. The morphology of ductile or brittle fracture can be determined based on the load vs. deflection curves received from the three-point bend test.

The fracture surface morphologies of the AM-FFF ABS specimens for the six examined configurations after the three-point bend tests are presented in figure 5. After the three-point bend test, a main difference in the fracture surface topography

was observed between the samples that failed, mainly through the layers (flat and on-edge orientation) and the samples breaking in between the layers (upright orientation). The flat and on-edge configurations result in a relatively rough surface topography (Fig. 5a-d), exhibiting the roughest morphology for flat $-45^\circ/+45^\circ$ samples (Fig. 5b). The upright $0^\circ/90^\circ$ configuration shows crack propagating between the layers along the 0° rasters and at halfway, switching to the adjacent layer to propagate along the 90° rasters (Fig. 5e). The upright $-45^\circ/+45^\circ$ raster orientation shows a typical brittle fracture with relatively smooth morphology, through a single propagating crack in between two adjacent layers (Fig. 5f).

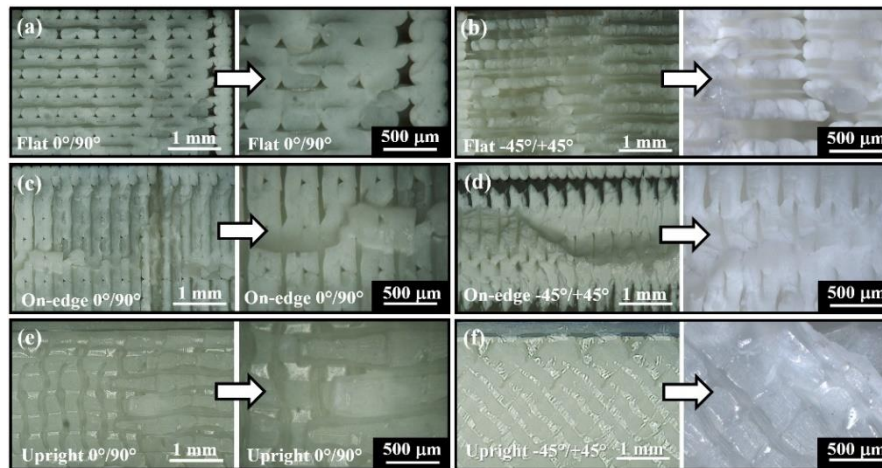


Fig. 5. High magnification optical LM photographs of the AM-FFF ABS specimens after a three-points bend tests, showing the detailed views of the modes of fracture and crack propagation for six different build strategies: a) flat $0^\circ/90^\circ$ specimen; b) flat $-45^\circ/+45^\circ$ specimen; c) on-edge $0^\circ/90^\circ$ specimen; d) on-edge $-45^\circ/+45^\circ$ specimen; e) upright $0^\circ/90^\circ$ specimen; f) upright $45^\circ/+45^\circ$ specimen

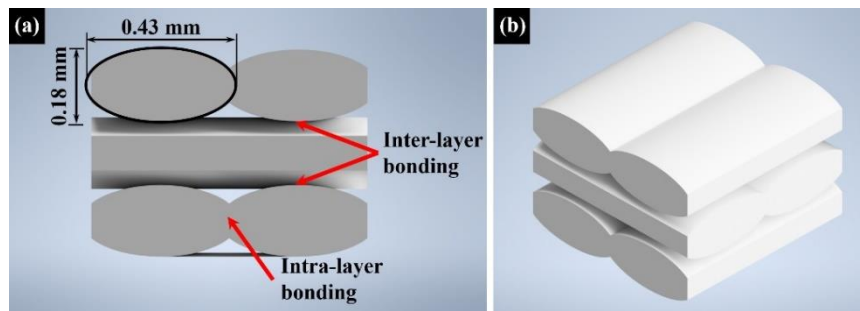


Fig. 6. CAD model visualization of the $0^\circ/90^\circ$ building configuration unit cell, showing the fibers and the weld between the fibers located at the same layer (intra-layer weld) and the weld between two adjacent layers (inter-layer weld): a) front view; and b) isometric view

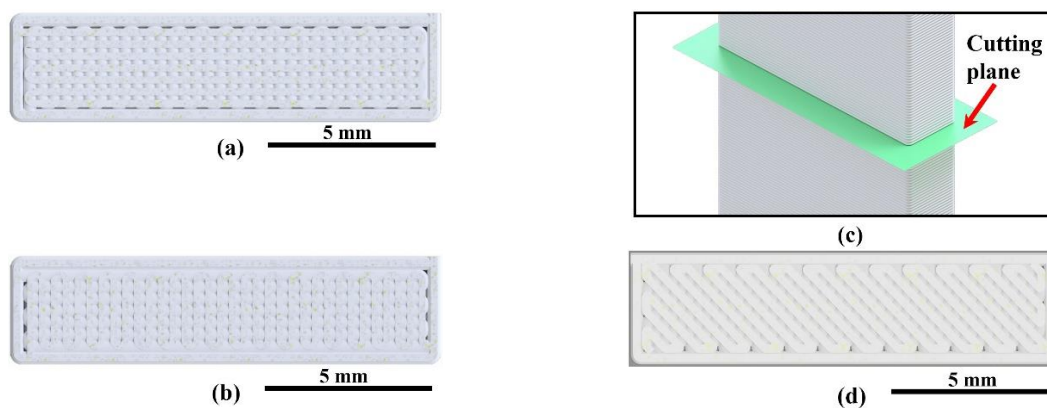


Fig. 7. CAD model visualization of the upright $0^\circ/90^\circ$ and $-45^\circ/+45^\circ$ configurations: a) cut between two adjacent layers in the upright $0^\circ/90^\circ$, where the welds of 0° rasters layer are shown on top of 90° rasters layer; b) the cut between two adjacent layers in the upright $0^\circ/90^\circ$, where the welds of 90° rasters layer shown on top of 0° rasters layer; c) a cutting plane; d) upright $-45^\circ/+45^\circ$ model cut between two adjacent layers, where the welds of -45° rasters layer are shown on top of the $+45^\circ$ rasters layer

3.4. Structure Visualization

The CAD model visualization of the $0^\circ/90^\circ$ building configuration unit cell (Fig. 6a-b) illustrates the orientations of the 0° and 90° rasters, the weld

between the rasters located at the same layer (intra-layer bond), and the weld between two adjacent layers (inter-layer bond).

The CAD model visualization of the upright $0^\circ/90^\circ$ building configuration illustrates the CS

between two adjacent layers, where the bonds of the 0° rasters layer are shown on top of the 90° rasters layer (Fig. 7a), and the CS between two adjacent layers, where the welds of the 90° rasters layer are shown on top of the 0° rasters layer (Fig. 7b). A CAD model visualization of a typical CS plane of the upright building configurations is illustrated in figure 7c. The CAD model visualization of the upright $-45^\circ/+45^\circ$ building configurations illustrates the CS plane between two adjacent layers, where the welds of the -45° rasters layer are shown on top of the $+45^\circ$ rasters layer (Fig. 7d).

The visualization of the flat $0^\circ/90^\circ$ configuration illustrates the cutting plane through the center of the 90° rasters layer (Fig. 8). It also illustrates the CS through the center of the 90° rasters layer fibers (Fig. 9a) and the CS through the welds between two adjacent fibers of the 90° rasters layer (Fig. 9b). The CAD model visualization of the flat $-45^\circ/+45^\circ$

configuration illustrates the CS through the center of the model (Fig. 10a) and the CS 1 mm distance from the center of the model (Fig. 10b). The CAD model visualization of the on-edge $-45^\circ/+45^\circ$ configuration illustrates the CS through the center of the model (Fig. 10c), and the CS 1 mm away from the center of the model (Fig. 10d).

The CAD model visualization of the on-edge $0^\circ/90^\circ$ configuration illustrates the CS through the center of the 90° rasters layer (Fig. 11a) and the CS through the welds between two adjacent fibers of the 90° rasters layer (Fig. 11b). The CAD model also illustrates the crack propagation path for the different build strategies, including the typical fracture surface morphologies for the flat $0^\circ/90^\circ$ configuration (Fig. 12a), the flat $-45^\circ/+45^\circ$ configuration (Fig. 12b), the on-edge $0^\circ/90^\circ$ configuration (Fig. 12c), and the on-edge $-45^\circ/+45^\circ$ configuration (Fig. 12d).

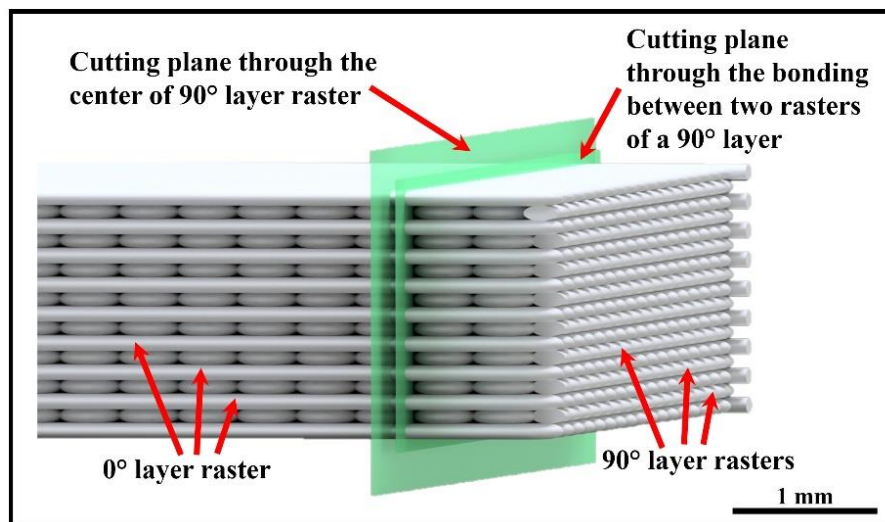


Fig. 8. CAD model visualization of the flat $0^\circ/90^\circ$ configuration (contour rasters not included), showing the cutting plane through the center of the 90° rasters layer

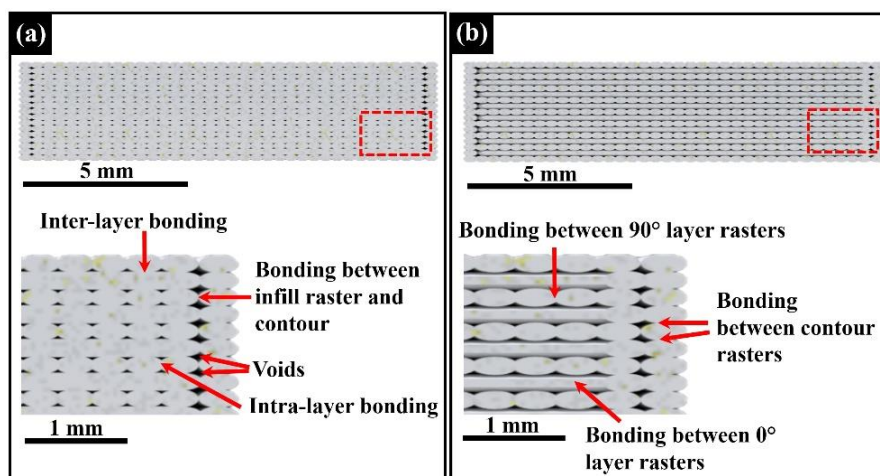


Fig. 9. CAD model visualization of the flat $0^\circ/90^\circ$ configuration: a) CS through the center of 90° rasters layer; b) CS through the welds between two adjacent rasters of 90° rasters layer

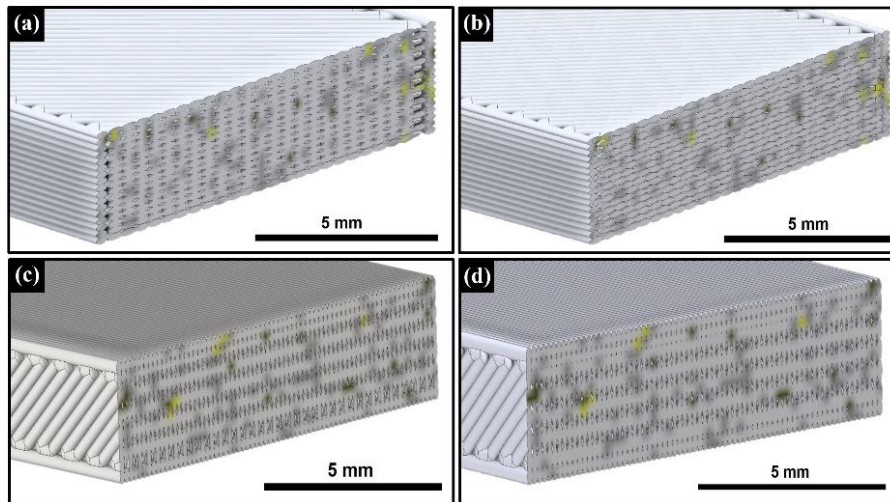


Fig. 10. CAD model visualization (isometric view) of the: a) flat $-45^{\circ}/+45^{\circ}$ configuration, cut through the center of the model; b) flat $-45^{\circ}/+45^{\circ}$ configuration, CS 1 mm away from the center of the model; c) on-edge $-45^{\circ}/+45^{\circ}$ CAD model cut through the center of the model; d) on-edge $-45^{\circ}/+45^{\circ}$ configuration CS 1 mm away from the center of the model

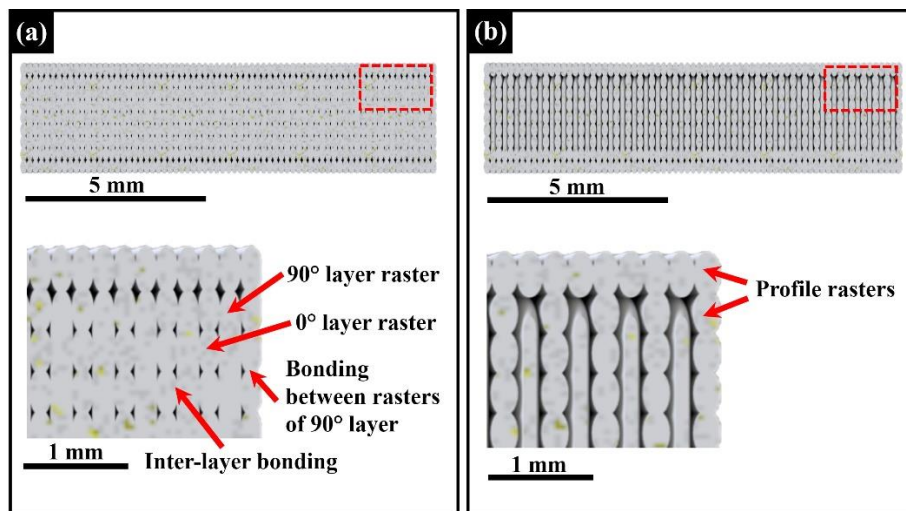


Fig. 11. On-edge $0^{\circ}/90^{\circ}$ CAD model visualization of: a) a cut through the center of 90° rasters layer; b) a cut through the welds between two adjacent rasters of 90° rasters layer

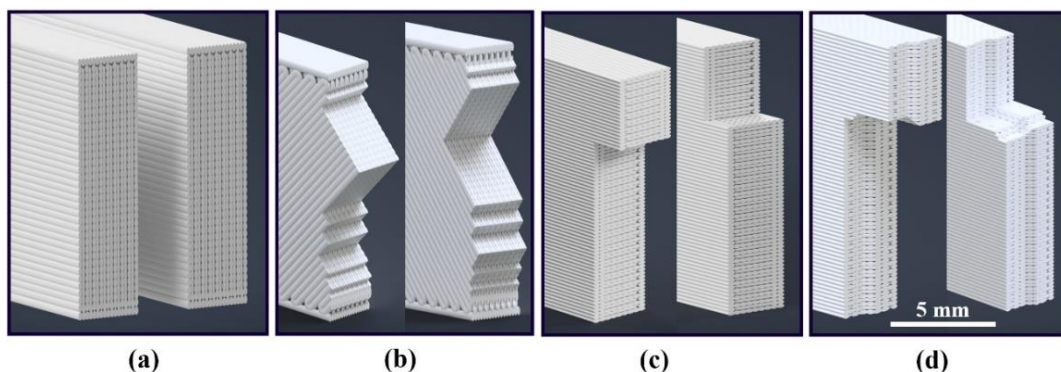


Fig. 12. CAD model visualization (isometric view) of the fracture for different build strategies additively manufactured ABS: a) the two sides of the fractured surface of the flat $0^{\circ}/90^{\circ}$ configuration; b) the two sides of the fractured surface of the flat $-45^{\circ}/+45^{\circ}$ configuration; c) the two sides of the fractured surface of the on-edge $0^{\circ}/90^{\circ}$ configuration; d) the two sides of the fractured surface of the on-edge $-45^{\circ}/+45^{\circ}$ configuration

3.5. Delamination and Crack Propagation

TLF (Appendix A, Fig. A2) was used to analyze the physical response behavior of the specimens during the bend test. Highly whitened diffuse zones appeared on the lower edge of all test specimens and propagated in the direction of the bending load. In all the flat and on-edge samples ($0^\circ/90^\circ$ and $-45^\circ/+45^\circ$ configurations), a symmetric pattern of thick white lines of different lengths was always created on both sides of the crack path, about 10 mm on each side of the crack's location (Fig. 13). The thick white lines are typically spaced equally around the crack path.

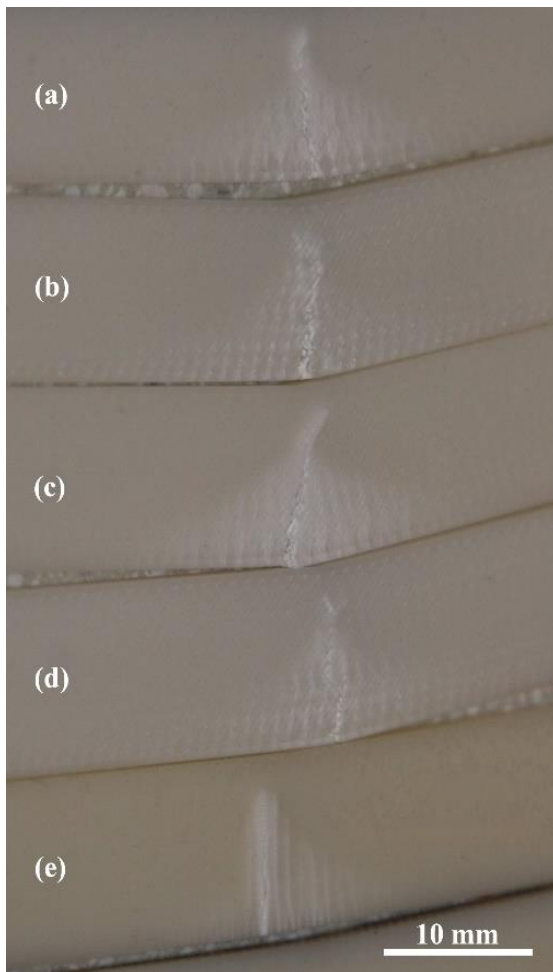


Fig. 13. The AM-FFF ABS photos of post-bending specimens, printed with different hatching strategies; the bend test was stopped before final failure. Shown are typical symmetric patterns of deformation bands parallel to crack propagation direction: a) flat $0^\circ/90^\circ$; b) flat $-45^\circ/+45^\circ$; c) on-edge $0^\circ/90^\circ$; d) on-edge $-45^\circ/+45^\circ$; e) upright $0^\circ/90^\circ$

Figure 14a-c exhibits typical TLF views of the crack “jumping” over from one layer to an adjacent layer in a flat $-45^\circ/+45^\circ$ specimen, the initiation and tip of a crack propagating in the flat $-45^\circ/+45^\circ$ specimen and the crack cutting through the layers in a flat $-45^\circ/+45^\circ$ specimen.

4. RESULTS AND DISCUSSION

The results of the study demonstrate that the mechanical properties of the upright specimens are mainly dictated by the bonding between the layers and are marginally influenced by the in-plane rasters' orientation. The on-edge and flat mechanical properties are determined both by the strength of the rasters and by the bonding between the adjacent rasters, leading to the substantial influence of the in-plane raster angles, as the failure is of the intra-layer type.

This research introduces an integrated approach in order to understand the strength of ABS parts produced by AM-FFF. These are based on the observations that were performed following the mechanical testing, to detect the quality of the printed surfaces, including possible defects and morphology of the fracture, as well as to visualize fracture surface morphology and crack propagation paths. The current results add significant knowledge regarding the overall mechanical response of the ABS specimens processed through FFF and will be useful in engineering design applications of structural parts, as explained below.

4.1. Density, Dimensions, and Discontinuities

Dimensional changes compared to the CAD dimensions generally occur in AM-FFF printed parts. Typically, in the case of AM-FFF ABS parts there is a decrease in dimensions (shrinkage) in the horizontal X and Y-directions of the build platform, but growth in dimension (expansion) in the vertical Z-direction; hence, the build strategy has a significant effect on the dimensional accuracy of the printed parts [47] – [49]. In the current study, a satisfactory agreement was attained between the dimensions of the printed specimens and the nominal CAD values. In all six configurations, a relatively small expansion was observed in most of the samples. The mean values of the deviation (%) of the specimens' thickness (3.2 mm), height (12.7 mm) and length (127) from the designed CAD dimensions were 1.2%, 0.7% and 0.3%, respectively (Table 2).

The materials created by the AM-FFF technique are laminate composites with governable structural features associated with the deposited polymer filament layout and void geometry [28], [29], [33] – [35]. Porosity is inherent in the current AM-FFF technology because the components are built from deposited polymer filaments with ellipsoidal characteristics that do not pack into an entirely dense volume. Relatively long and/or short empty gaps remain between filaments, both in between the layers and within the built layers. The residual porosity depends on the build-strategy, leading to lower mechanical properties than of bulk thermoplastic polymer. The density measurements analysis showed that upright specimens exhibited the lowest density (about 90%), while the on-edge specimens displayed the highest density (above 96%), matching the highest mechanical properties.

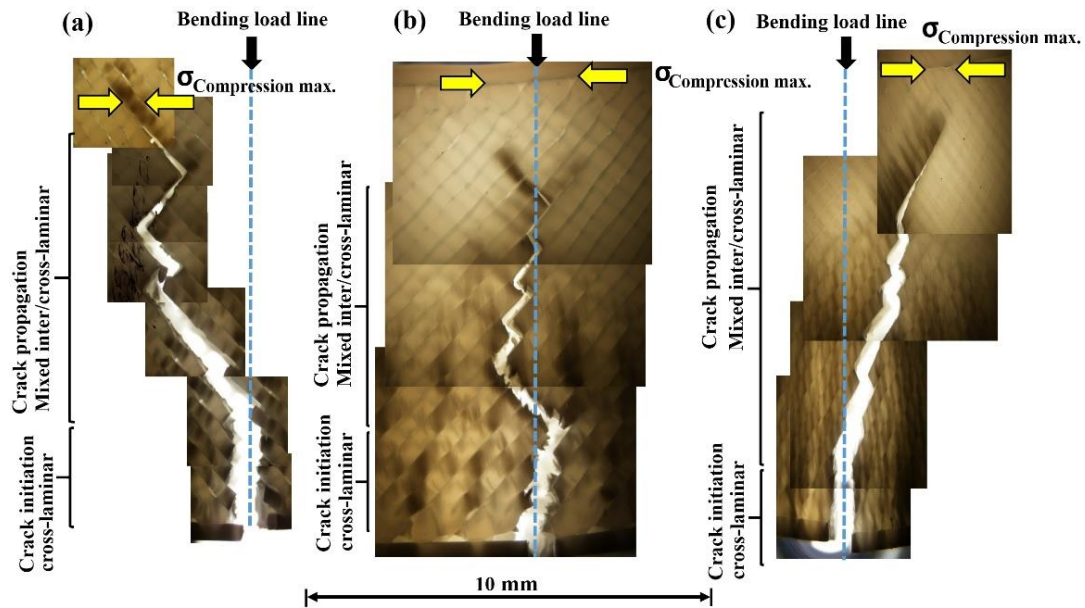


Fig. 14. Photographic sequences utilizing the transmitted light microscopy system showing the crack propagation behavior throughout the AM-FFF ABS specimen [24], where the bending was stopped shortly prior to complete failure of the specimen: a)-c) observation of the crack propagation path of three tested specimens

There are a few major mechanical challenges that should be considered and overcome in the field of topology optimization of AM-FFF technique, among them the material anisotropy and weakness along build direction [14], [15].

Macro and microstructural discontinuities, like voids, play an important role in fracture initiation and cracking, especially in the brittle fracture mode. Voids may serve as crack nucleation spots or even as crack-arrestors, as they may blunt the tip of a crack as it crosses the void. Structure anisotropy is created at a mesostructured scale as the filament deposition direction changes layer-by-layer, producing different shapes of voids such as triangular, diamond and circular ones between adjacent rasters. Certain regions within the samples are likely to become probable sites for void creation, such as locations between the contour and deposited rasters; limited porosity also formed in and in-between the bonded regions.

4.2. Mechanical Properties

When analyzing the load vs. deflection curves, two major groups are observed that have different mechanical responses to the loading in three-point bending: flat and on-edge specimens sustain higher loads and yield higher deflection by far, compared to upright specimens. Flat and on-edge specimen curves display elastic zones ending with elastic-plastic zones, with some degree of strain hardening towards the ultimate bending load (UBL) and finally, the load drops towards the failure load. The elastic-plastic zone is typically observed after 2 mm of loading nose displacement, as indicated on the load vs. deflection curves, as well as visible whitening (crazing) ahead of the crack tip. On the other hand, the upright specimens'

bending curves show only a close to linear elastic zone, ending in a much lower UBL and failing at the UBL (Appendix A, Fig. A3). Flat and on-edge build orientations have quite close FMEs, comparing to a much lower FME for upright specimens (Table 5).

For the ABS upright specimens, the rupture occurs in an inter-layer manner displaying a fair flat fracture morphology with a FME of about 1.45 GPa. The flat and on-edge specimens fail mainly in an intra-layer mode, exhibiting relatively rough fracture morphologies and displaying a FME of about 2.0 GPa. The on-edge specimens exhibited the highest mechanical properties, whilst the $0^\circ/90^\circ$ samples showed some advantage over the $-45^\circ/+45^\circ$ specimens. The slightly higher FME and FS of the on-edge $0^\circ/90^\circ$ samples can be associated with the quantity and shape of voids and the presence of gaps between the rasters, as they probably serve as crack arrestors and blunt the crack's tip.

The overall mechanical properties obtained in this research for the $0^\circ/90^\circ$ and $-45^\circ/+45^\circ$ orientations raster angles are a mixture of the whole specimen layer properties. For example, the average deflection and flexural strength of the on-edge $0^\circ/90^\circ$ orientation are 4.9 mm and 70.4 MPa, respectively and those of the on-edge $-45^\circ/+45^\circ$ are 5.0 mm and 65.4 MPa, respectively. The average deflection and flexural strength of the flat specimens for the $0^\circ/90^\circ$ are 3.2 mm and 58.3 MPa and of the flat $-45^\circ/+45^\circ$ are 5.4 mm and 62.8 MPa, respectively (Table 5). The results showed that the in-plane raster angle significantly influences the mechanical properties of both on-edge and flat specimens. The on-edge and flat mechanical properties are dictated both by the raster strength and the bonding between the adjacent rasters, leading to a substantial influence of the in-plane raster angles;

therefore, the failure is mostly of the intra-layer type. The average mechanical properties of the upright $0^\circ/90^\circ$ specimen are 1.5 mm and 24.2 MPa and those of the upright $-45^\circ/+45^\circ$ are 1.4 mm and 24.8 MPa (Table 5). Insignificant differences between the $0^\circ/90^\circ$ and $-45^\circ/+45^\circ$ were observed for the upright orientation, leading to the conclusion that the in-plane raster angle slightly, if at all, influences the mechanical properties, if at all. The mechanical properties of the upright specimens are mainly dictated by the bonding between the laminae and are marginally influenced by raster orientation; the failure is definitely of the inter-layer type. In this case, the laminae's mechanical properties are less important than the interlayer bonding. The current results clearly show that the overall mechanical response is related to the mode of failure; interlayer failure for the upright specimens and mainly intra-layer failure for both on-edge and flat specimens.

The experimental results show that the FS and deflection change significantly for the samples printed ($-45^\circ/+45^\circ$) on different angles to the XY plane (Fig. 2b). The largest difference is between the 0° and 75° , i.e., the FS and the deflection are the largest for the 0° and 15° orientations, followed by the 30° , 45° , 60° , and 75° orientations in descending order (Fig. 3b, 3c). Each of the examined angles exhibited a different pattern of crack propagation during the test. As expected, the high-angle specimens failed by interlaminar crack propagation, while the failure of the low-angled bend test specimens was a consequence of mixed cross-laminar and interlaminar cracking (Fig. 3a).

AM-FFF ABS specimens exhibit strong anisotropic mechanical properties, as shown in tables 5-6 and figures 3-5, and the lowest deflection and lowest FS were found in the upright configuration (Fig. 4). Poor bonding (imperfect weld lines) between rasters located in between the layers and residual porosity are the main causes of low AM-FFF ABS mechanical properties printed in the Z-direction. For high-quality bonding to take place, the adjacent local volume of material within each raster must have sufficient time, at an adequate temperature, to enable polymer chains to diffuse and entangle across the interface.

As indicated by the manufacturer (Table 1), the flexural strength is higher than the tensile one. In addition, process parameters, such as printing temperature and deposition velocity, tend to influence the solid-state bond-forming processes, as well as the mechanical properties [6], [50].

4.3. Fractography

When AM-FFF ABS specimens are characterized, it is important to examine their fracture surface morphology in order to understand whether the experimental results match the expected fractographic theories [51]. The current fractographic analysis confirmed the presence

of different types of expected discontinuities on the fracture surfaces, such as voids and air gaps [7], [13]. Since these defects influence the mechanical properties and fracture behavior of the printed specimens and decrease their strength, suitable efforts are needed to reduce or eliminate such defects [7].

The failure mechanism of the upright specimens is layer separation because the bending load is applied parallel to the layers and the interface between adjacent laminae carries the bending load, not the rasters. The crack starts at the maximum stress (24.2 MPa for upright $0^\circ/90^\circ$ and 24.8 MPa for upright $-45^\circ/+45^\circ$) and leads to the fast, brittle failure of the specimens.

In the case of flat and on-edge specimens, the bending load is applied perpendicular to the layers' layout and the stresses act on both the rasters and the welds between rasters, i.e., the mechanical properties of these specimens are determined by the strength of both the rasters' material and weld lines between the rasters. The video taken during the bending tests shows that the crazing starts at the beginning of the elastic-plastic region and grows until a visible crack starts at the maximum stress (58.3 MPa for flat $0^\circ/90^\circ$, 62.8 MPa for flat $-45^\circ/+45^\circ$, 70.4 MPa for on-edge $0^\circ/90^\circ$ and 65.4 MPa for on-edge $-45^\circ/+45^\circ$) at the lowest region of the specimen.

The fracture energy needed for delamination of bonded ABS rasters in between the printed layers and inside the layers is much lower than the energy needed for the rupture of the filaments themselves. The layers of printed samples undergoing the three-point bend test are subjected to tensile stresses if they are below the mid-plane and to compressive stresses if they are above the mid-plane. As expected, the fractographic examination showed that all tested ABS samples failed by cracking the lowest specimen layer subjected to maximal tension stresses. The upright specimens fractured in an inter-layer mode, displaying close to flat fracture morphologies with a FME of approximately 1.4 to 1.5 MPa, while for the flat and on-edge specimens, the failure occurs mainly in the intra-layer mode, exhibiting relatively rough fracture morphologies and having a higher FME, about 1.9 to 2.1 MPa (Fig. 5a-f).

The current results indicate that the flat and on-edge specimens fail through a ductile fracture, whereas the upright configuration fails through a brittle fracture. According to the literature, failure which shows a ductile fracture manner, as observed for the flat and on-edge configurations, involves void growth and coalescence mechanisms followed by drawing and ductile tearing of fibrils [12]. The fractographic analysis of the upright samples leads to the conclusion that the brittle behavior is caused by the mesostructure properties of the as-built specimen i.e., by inherent weak inter-layer raster bonding zones containing significant inter-laminar discontinuities. The fracture always started in the lowest layer with the crack initiation location situated at the weakest

inter-laminar zone, containing stress risers such as unbonded sites. A slightly different fracture morphology was found in the upright $0^\circ/90^\circ$ samples. The larger voids in the $0^\circ/90^\circ$ samples lead to inter-filament bond failure and trigger crack propagation along the inter-laminar surface; they occasionally initiate an intra-layer crack cross-over from the initial layer to an adjacent one, creating a slightly rougher fracture surface. This phenomenon leads to insignificant changes in the mechanical properties, the FME slightly increasing to about 1.5 GPa, the FS slightly decreasing to 24.5 MPa, while almost no change was observed in the deflection values.

For the flat and on-edge specimens, the cross-layer fracture begins at the weakest filament, located inside the layer subjected to maximal tensile stresses, and the fracture propagates in an intra-layer mode until the specimen fails. The failure mode can be described as a mixture of failure of the intra-layer ABS filaments accompanied by brittle debonding of adjacent fibers. Debonding was found to be located at inherent weak filament bonding regions while the presence of intra-layer and inter-layer porosity played a major role in the surface morphology appearance. During the bend loading, the tensile stress in the adjacent uncracked layer continues to increase and the crack driving force increases. Occasionally, the propagating crack front splits up into few smaller cracks, leading to the failure of the succeeding weakest filaments or intra-layer filament bonds. This behavior leads to trans-filament crack propagation along the intra-layer surface, accompanied by a change in the crack path from a trans-filament path to a trans-bond path, based on energy considerations creating the inter-bond surfaces along the welded filaments. This was clearly observed in the flat and on-edge $-45^\circ/+45^\circ$ samples.

A significantly different crack path and fracture morphology was observed for the flat $0^\circ/90^\circ$ samples when compared to the flat $-45^\circ/+45^\circ$ samples. The general view of the crack path, after the failure, showed that the flat $-45^\circ/+45^\circ$ samples displayed a zigzag path of fracture along the specimen CS (Fig. 12b), while the flat $0^\circ/90^\circ$ samples displayed a relatively smooth and featureless fracture surface along the entire specimen CS (Fig. 12a). This mode of rupture (Fig. 12b) was initiated by the selective debonding of intra-layer filaments in -45° or $+45^\circ$ orientations; the rupture morphology of the flat $0^\circ/90^\circ$ samples was entirely different since the surface created by the selective debonding of intra-layer filaments was parallel to the specimen's CS surface and load direction.

Crack initiation sensitivity was examined by bend testing of two sets of as-printed samples (on-edge type): one set having the lowest layer subjected to maximal tension stresses, facing the support material, and a second set with the lowest layer facing the print nozzle, i.e., the last printed layer. No significant difference was observed in the mechanical

properties of both sets of ABS plus© samples processed on the Dimension Elite© FFF printing machine.

The three-point bend test generates tension on the low surface, opposite the load application side, and compression on the other surface of the specimen, producing a gradient in stress through the thickness of the sample. This causes the fracture surface to have some characteristics that are different from fracture surfaces produced in uniaxial tension. The rupture plane at the fracture initiation area is often perpendicular to the axis of maximum tensile stress but in some instances can show a zigzag pattern, depending on the local material's toughness level.

On-edge samples typically have some characteristic macroscale features that are absent in flat printed samples. Cracking starts on, or close to, the surface in tension and the crack moves into the lower tension region and towards the compression side. Figures 5c-d and 12c-d show a typical on-edge sample broken in bending; the fracture was initiated in a plane that was normal to the direction of tension. As the fracture progressed towards the compression side of a bending failure, the local stress state changed, causing the crack to wander out of its original plane. The crack sharply deflected from the perpendicular plane and slightly propagated along an inter-layer surface (Fig. 12c-d). The final failure occurred in the former compression region, where the crack typically redirected along the initial perpendicular plane and the specimen suddenly broke. This produced a lip or curl located on the compression side, commonly called the cantilever curl [52].

The failure mode observed in all printed samples, both in the layers subjected to tension or to compression stresses, was a mixture of failure of the notch-sensitive ABS material rasters accompanied by brittle debonding of adjacent bond rasters; the intra-layer and inter-layer porosity present in all printed samples played a significant role in the brittle fracture of the samples.

The material brittle failure was the result of an intrinsic mechanical response of the notch-sensitive ABS polymer containing low scattered porosity to bending stresses, accompanied by brittle debonding of adjacent rasters attached inside the layers and in between the layers.

Future SEM observation of the AM-FFF ABS specimens' fracture surface could add further information concerning the fracture modes and mechanisms [7], [12], [29], [39], [51].

4.4. Structure Visualization

The fracture CAD models developed in this study are powerful tools that help to understand the failure mechanisms of the ABS specimens printed by FFF technology. For upright build orientation, the relative density of the CAD model is within the relative

density range of the actual printed specimens. For flat and on-edge specimens, the relative density of the CAD model is about 5% lower than that of the printed specimen, due to the lower infill level of the CAD models compared to printed specimens. Most likely, when the printing head changes the movement direction (infill fibers, close to contour), there is a local slowdown, while the extruder continues to release material at a constant rate. Therefore, along the path line where the movement velocity of a print head is lower, more material is locally released. Therefore, in these places (i.e., connections between the infill fibers and the contour fiber) a good infill is obtained in the printed specimens, while, for CAD models, the infill is uniform along the entire print head trajectory. This is more significant for the flat and on-edge orientations since there are more interactions between the infill fibers and the contour fibers, especially for $-45^{\circ}/+45^{\circ}$ specimens.

In addition, according to microscopic images, the CS of a raster has a rectangular shape with rounded corners, rather than the perfect elliptical shape used in the CAD models. While printed, the material is extruded in the form of a round section thread with a diameter equal to the diameter of the nozzle, but it "spreads" to the sides when placed on top of a previous layer. The resulting shape creates smaller voids between rasters when compared to the CAD models, resulting in an improved infill and at a relatively higher density (Fig. 5).

4.5. Delamination and Fracture Pathing

In the fully loaded state, whitening appears in front of the crack tip, confirming the elastic-plastic response of ABS material (Fig. 13 and Fig. 14). The symmetric pattern of thick white lines formed parallel to the loading line is associated with the crazing behavior of ABS material (stress fields are visible ahead of the crack tip). Occasionally, the test was stopped just before the specimen's failure to allow a complete view of the white line patterns. Crazing is a tensile deformation phenomenon of high molecular weight glassy polymers, where amorphous polymer chains realign in the direction of force; the craze walls form perpendicular to the direction of the maximum tensile principal stress. The length of the white lines, a few hundred microns apart, changes approximately linearly, forming a triangular pattern in the crack vicinity. The substantial whitening in the crack area is the result of crazing in the ABS material during elastic-plastic deformation, while the sample is stressed.

To visualize and further understand the crack propagation behavior in AM-FFF ABS under bending load, several specimens were examined during the test, which was stopped before the final failure. For the flat $-45^{\circ}/+45^{\circ}$ specimen, the initial crack reached an inter-layer region where it departed from coplanarity, with the initial crack and kinks, towards a region of lower toughness to propagate in an

interlaminar mode, displaying a zigzag pattern of fracture (Fig. 12b and 14). This method made it possible to closely examine the total length of the crack, from its initiation to its tip, before the specimen failed. All three specimens showed the same crack initiation and propagation behavior (Fig. 14a-c): (a) the crack started at the lower region of the bending specimen, at maximum tensile stress, (b) crack initiation occurred in a cross-laminar mode, (c) the crack propagated in a mixed inter and cross laminar manner. Close to failure, the crack narrowed and propagated through an area with residual compressive stresses displaying highly visible stressed areas near the crack tip (Fig. 14).

5. CONCLUSIONS

- The experimental results showed that upright specimens exhibited the lowest density and the lowest mechanical properties, while the on-edge specimens displayed the highest densities and the highest mechanical properties (Table 5). In addition, the results indicated that the high-angle specimens had lower flexural strength (Table 6). Hence, changing the specimens' build strategy, as shown by the selected six configurations, as well as the different six building angles that affect the density as well as the mechanical properties of the 3D-printed ABS. The anisotropy of the FFF ABS is quantitatively shown in tables 5 and 6, and qualitatively described by figures 3a, 5 and 12.
- Crack propagation and failure modes are dissimilar for the different examined AM-FFF configurations. Overall, there are two main failure modes for the AM-FFF ABS three-point bend tested specimens: (1) inter-layer/inter-raster fusion bond failure, which is the main contributor to the failure of all upright samples and (2) intra-layer trans-raster and inter-raster failures, which are the main contributors to the failure of the flat and on-edge specimens.
- No uniform distribution of stresses or material homogeneity can be achieved in the AM-FFF ABS specimens. Certain regions within the samples are expected to probably become sites of crack initiation due to either higher tensile stresses and/or higher-than-average crack sensitivity that can lead to a brittle failure mode.
- Both $0^{\circ}/90^{\circ}$ and $-45^{\circ}/+45^{\circ}$ upright samples displayed a brittle inter-layer failure, caused by the printed material macrostructure that exhibited very low mechanical properties. The $0^{\circ}/90^{\circ}$ and $-45^{\circ}/+45^{\circ}$ on-edge samples exhibited the highest mechanical properties whilst the $0^{\circ}/90^{\circ}$ samples showed some advantage over the $-45^{\circ}/+45^{\circ}$ specimens. The density measurements analysis showed that both $0^{\circ}/90^{\circ}$ and $-45^{\circ}/+45^{\circ}$ upright samples exhibited the lowest density, consistent with the samples' low mechanical properties, while the $0^{\circ}/90^{\circ}$ and $-45^{\circ}/+45^{\circ}$ on-edge samples

displayed the highest densities, matching the highest mechanical properties. In the future, it would be interesting to examine the mechanical properties of specimens with different raster orientations, such as $-30^{\circ}/+30^{\circ}$. However, this is beyond the scope of the current study.

- The fracture energy needed for breaking the bonds in between rasters is much lower than the energy needed for the rupture of the rasters themselves. This is the main driving factor behind the mechanical properties and fracture characteristics of ABS printed material when using different print strategies. The lowest fracture energy needed to break the bend test specimens is the one needed to create fractures containing debonded surfaces and porosity, as observed in all the upright specimens.
- A whitening appearance resulting from a localized change in ABS refractive index (transmitted light scattering) was observed during the three-point bend tests on the on-edge and flat specimens. Micro-voids of dimensions, equal to or greater than the wavelength of light, were the primary source of stress whitening. Whitening formation preceded the crack initiation, occurring under the plane-strain conditions created by non-uniform stress distribution near stress risers, present in the printed ABS polymer.
- Based on energy considerations, discontinuities such as voids play a significant part in fracture initiation and may serve as crack nucleation zones. Since AM-FFF ABS materials are anisotropic by their nature, the fractographic images (Fig. 5) of the different specimen configurations are significantly different. For each configuration the crack will propagate in the path providing the surface energy that is essential to generate the newly formed crack surfaces, usually resulting in failure dominated by mode I fracture. Yet, future SEM analysis of the current AM-FFF ABS specimens' fracture surface may add additional information concerning the fracture modes and mechanisms.
- The failure mode observed in all printed specimens was the result of the intrinsic mechanical response of the printed ABS polymer containing low scattered porosity to bending stresses, accompanied by brittle debonding of adjacent welded rasters inside the layers and in between the layers.

ABBREVIATIONS

ABS – Acrylonitrile butadiene styrene
 AM – Additive manufacturing
 CAD – Computer aided design
 CS – Cross-section
 F – Flat configuration
 FFF – Fused filament fabrication
 FME – Flexural modulus of elasticity

FS – Flexural strength
 LM – Light microscope
 OE – On-edge configuration
 SEM – Scanning electron microscope
 TLF – Transmitted-light fractography
 UBL – Ultimate bending load
 UR – Upright configuration
 VT – Visual testing

LIST OF SYMBOLS

b – Width of the three-point bend testing specimen's cross-section [mm]
 F – Applied force [N]
 h – Height of the three-point bend testing specimen's cross-section [mm]
 L – Distance between the two anvils of the tensile and compression tester universal testing machine [mm]
 l – Length of the three-point bend testing specimen [mm]
 δ – Deflection [mm]
 ρ_{ABS} – Density of ABS material [g/cm^3]
 ρ_{CAD} – Density of the CAD models [g/cm^3]
 $\rho_{\text{CAD}}\%$ – Relative density of the CAD models [%]
 $\rho_{\text{AM-FFF}}$ – Density of printed specimens [g/cm^3]
 $\rho_{\text{AM-FFF}}\%$ – Relative density of printed specimens [%]
 σ – Flexural strength [MPa]
 σ_b – Flexural strength of a beam [MPa]
 σ_y – Yield strength [MPa]
 E_{FME} – Calculated flexural modulus of elasticity [MPa]

ACKNOWLEDGEMENTS

The authors would like to thank A. Ulanov, N. Dresler, A. Solomon, D. Shabat, S. Maman, and N. Bilenkin, from the School of Mechanical Engineering, Afeka Academic College of Engineering, for their engineering and technical assistance. Thanks are also due to M. Cohen and D. Cvikel from the Leon Recanati Institute for Maritime Studies and Department of Maritime Civilizations, University of Haifa, for their assistance and to D. Sherman from the School of Mechanical Engineering, Tel Aviv University for his contribution. The authors are also grateful to B. Doron for the English editing.

REFERENCES

- [1] Gewelber O., Rosenthal Y., Ashkenazi D., Stern A., *Mechanical properties, structure and fracture behavior of additive manufactured FFF-ABS specimens*, Annals of "Dunarea de Jos" University of Galati. Fascicle XII, Welding Equipment and Technology, vol. 31, 2020, pp. 71–78, <https://doi.org/10.35219/awet.2020.11>.
- [2] Wickramasinghe S., Do T., Tran P., *FDM-based 3D printing of polymer and associated composite: A review on mechanical properties, defects and treatments*, Polymers, vol. 12, iss. 7, 2020, p. 1529, <https://doi.org/10.3390/polym12071529>.
- [3] Penumakala P. K., Santo J., Thomas A., *A critical review on the fused deposition modeling of thermoplastic polymer composites*, Composites Part B: Engineering, vol. 201, 2020, p. 108336, <https://doi.org/10.1016/j.compositesb.2020.108336>.

- [4] Goh G. D., Yap Y. L., Tan H. K. J., Sing S. L., Goh G. L., Yeong W. Y., *Process-structure-properties in polymer additive manufacturing via material extrusion: A review*, Critical Reviews in Solid State and Materials Sciences, vol. 45, iss. 2, 2020, pp. 113–133, <https://doi.org/10.1080/10408436.2018.1549977>.
- [5] Cuan-Urquiza E., Barocio E., Tejada-Ortigoza V., Pipes R. B., Rodriguez C. A., Roman-Flores A., *Characterization of the mechanical properties of FFF structures and materials: A review on the experimental, computational and theoretical approaches*, Materials, vol. 12, iss. 6, 2019, p. 895, <https://doi.org/10.3390/ma12060895>.
- [6] Popescu D., Zapciu A., Amza C., Baciu F., Marinescu R., *FDM process parameters influence over the mechanical properties of polymer specimens: A review*, Polymer Testing, vol. 69, 2018, pp. 157–166, <https://doi.org/10.1016/j.polymertesting.2018.05.020>.
- [7] Khosravani M. R., Berto F., Ayatollahi M. R., Reinice T., *Fracture behavior of additively manufactured components: A review*, Theoretical and Applied Fracture Mechanics, vol. 109, 2020, p. 102763, <https://doi.org/10.1016/j.tafmec.2020.102763>.
- [8] Lay M., Thajudin N. L. N., Hamid Z. A. A., Rusli A., Abdullah M. K., Shuib R. K., *Comparison of physical and mechanical properties of PLA, ABS and nylon 6 fabricated using fused deposition modeling and injection molding*, Composites Part B: Engineering, vol. 176, 2019, p. 107341, <https://doi.org/10.1016/j.compositesb.2019.107341>.
- [9] Garzon-Hernandez S., Arias A., Garcia-Gonzalez D., *A continuum constitutive model for FDM 3D printed thermoplastics*, Composites Part B: Engineering, 2020, vol. 201, p. 108373.
- [10] Coasey K., Hart K. R., Wetzel E., Edwards D., Mackay M. E., *Nonisothermal welding in fused filament fabrication*, Additive Manufacturing, vol. 33, 2020, p. 101140, <https://doi.org/10.1016/j.compositesb.2020.108373>.
- [11] Hong Y., Mrinal M., Phan H., Tran V. D., Liu X., Luo C., *In-situ observation of the extrusion processes of Acrylonitrile Butadiene Styrene and Polylactic Acid for material extrusion additive manufacturing*, Additive Manufacturing, vol. 49, 2021, p. 102507, <https://doi.org/10.1016/j.addma.2021.102507>.
- [12] Verma P., Ubaid J., Schiffer A., Jain A., Martínez-Pañeda E., Kumar S., *Essential work of fracture assessment of acrylonitrile butadiene styrene (ABS) processed via fused filament fabrication additive manufacturing*, The International Journal of Advanced Manufacturing Technology, vol. 113, iss. 3, 2021, pp. 771–784, <https://doi.org/10.1007/s00170-020-06580-4>.
- [13] Butt J., Bhaskar R., *Investigating the effects of annealing on the Mechanical properties of FFF-printed thermoplastics*, Journal of Manufacturing and Materials Processing, vol. 4, iss. 2, 2020, p. 38, <https://doi.org/10.3390/jmmp4020038>.
- [14] Mirzendehtel A. M., Rankouhi B., Suresh K., *Strength-based topology optimization for anisotropic parts*, Additive Manufacturing, vol. 19, 2018, pp. 104–113, <https://doi.org/10.1016/j.addma.2017.11.007>.
- [15] Tronvoll S. A., Welo T., Elverum C. W., *The effects of voids on structural properties of fused deposition modelled parts: A probabilistic approach*, The International Journal of Advanced Manufacturing Technology, vol. 97, iss. 9, 2018, pp. 3607–3618, <https://doi.org/10.1007/s00170-018-2148-x>.
- [16] Garg A., Bhattacharya A., *An insight to the failure of FDM parts under tensile loading: finite element analysis and experimental study*, International Journal of Mechanical Sciences, vol. 120, 2017, pp. 225–236, <https://doi.org/10.1016/j.ijmecsci.2016.11.032>.
- [17] Riddick J. C., Haile M. A., Wahlde R., Cole D. P., Bamiduro O., Johnson T. E., *Fractographic analysis of tensile failure of acrylonitrile-butadiene-styrene fabricated by fused deposition modeling*, Additive Manufacturing, vol. 11, pp. 49–59, 2016, <https://doi.org/10.1016/j.addma.2016.03.007>.
- [18] Das A., McIlroy C., Bortner M., *Advances in modeling transport phenomena in material-extrusion additive manufacturing: Coupling momentum, heat, and mass transfer*, Progress in Additive Manufacturing, vol. 6, pp. 3–17, 2021, <https://doi.org/10.1007/s40964-020-00137-3>.
- [19] Cantrell J. T., Rohde S., Damiani D., Gurnani R., DiSandro L., Anton J., Young A., Jerez A., Steinbach D., Kroese C., Ifju P. G., *Experimental characterization of the mechanical properties of 3D-printed ABS and polycarbonate parts*, Rapid Prototyping Journal, vol. 23, iss. 4, 2017, pp. 811–824.
- [20] Bellehumeur C., Li L., Sun Q., Gu P., *Modeling of bond formation between polymer filaments in the fused deposition modeling process*, Journal of Manufacturing Processes, vol. 6, iss. 2, 2004, pp. 170–178, [https://doi.org/10.1016/S1526-6125\(04\)70071-7](https://doi.org/10.1016/S1526-6125(04)70071-7).
- [21] Sun Q., Rizvi G. M., Bellehumeur C. T., Gu P., *Effect of processing conditions on the bonding quality of FDM polymer filaments*, Rapid Prototyping Journal, vol. 14, 2008, pp. 72–80.
- [22] Shabat D., Rosenthal Y., Ashkenazi D., Stern A., *Mechanical and structural characteristics of fused deposition modeling ABS material*, Annals of "Dunarea de Jos" University of Galati. Fascicle XII, Welding Equipment and Technology, vol. 28, 2017, pp. 16–24.
- [23] Solomon A., Rosenthal Y., Ashkenazi D., Stern A., *Structure and mechanical behavior of additive manufactured fused deposition modeling ABS*, Annals of "Dunarea de Jos" University of Galati. Fascicle XII, Welding Equipment and Technology, vol. 29, pp. 2018, 47–56.
- [24] Rosenthal Y., Stern A., Treivish I., Ashkenazi D., *Crack propagation in flexural testing of additive manufactured acrylonitrile butadiene styrene*, Annals of "Dunarea de Jos" University of Galati. Fascicle XII, Welding Equipment and Technology, vol. 30, 2019, pp. 21–26.
- [25] Peterson A. M., *Review of acrylonitrile butadiene styrene in fused filament fabrication: A plastics engineering-focused perspective*, Additive Manufacturing, vol. 27, 2019, pp. 363–371, <https://doi.org/10.1016/j.addma.2019.03.030>.
- [26] Das A., Chatham C. A., Fallon J. J., Zawaski C. E., Gilmer E. L., Williams C. B., Bortner M. J., *Current understanding and challenges in high temperature additive manufacturing of engineering thermoplastic polymers*, Additive Manufacturing, vol. 34, 2020, p. 101218, <https://doi.org/10.1016/j.addma.2020.101218>.
- [27] Vidakis N., Petousis M., Velidakis E., Liebscher M., Mechtcherine V., Tzounis, L., *On the strain rate sensitivity of fused filament fabrication (FFF) processed PLA, ABS, PETG, PA6, and PP thermoplastic polymers*, Polymers, vol. 12, iss. 12, 2020, p. 2924, <https://doi.org/10.3390/polym12122924>.
- [28] Ahn S. H., Montero M., Odell D., Roundy S., Wright P. K., *Anisotropic material properties of fused deposition modeling ABS*, Rapid Prototyping Journal, vol. 8, iss. 4, 2002, pp. 248–257.
- [29] Beattie N., Bock N., Anderson T., Edgeworth T., Kloss T., Swanson J., *Effects of build orientation on mechanical properties of fused deposition modeling parts*, Journal of Materials Engineering and Performance, vol. 30, iss. 7, 2021, pp. 5059–5065, <https://doi.org/10.1007/s11665-021-05624-4>.
- [30] Wichniarek R., Hamrol A., Kuczek W., Górski F., Rogalewicz M., *ABS filament moisture compensation possibilities in the FDM process*, CIRP Journal of Manufacturing Science and Technology, vol. 35, 2021, pp. 550–559, <https://doi.org/10.1016/j.cirpj.2021.08.011>.
- [31] Jiang D., Smith D. E., *Anisotropic mechanical properties of oriented carbon fiber filled polymer composites produced with fused filament fabrication*, Additive Manufacturing, vol. 18, 2017, pp. 84–94, <https://doi.org/10.1016/j.addma.2017.08.006>.
- [32] Ayatollahi M. R., Nabavi-Kivi A., Bahrami B., Yahya M. Y., Khosravani M. R., *The influence of in-plane raster angle on tensile and fracture strengths of 3D-printed PLA specimens*, Engineering Fracture Mechanics, vol. 237, 2020, p. 107225, <https://doi.org/10.1016/j.engfracmech.2020.107225>.
- [33] Rajpurohit S. R., Dave H. K., *Flexural strength of fused filament fabricated (FFF) PLA parts on an open-source 3D printer*, Advances in Manufacturing, vol. 6, iss. 4, 2018, pp. 430–441, <https://doi.org/10.1007/s40436-018-0237-6>.
- [34] Garzon-Hernandez S., Garcia-Gonzalez D., Jerusalem A., Arias A., *Design of FDM 3D printed polymers: An experimental-modelling methodology for the prediction of mechanical properties*, Materials & Design 188, 2020, p. 108414, <https://doi.org/10.1016/j.matdes.2019.108414>.
- [35] Dialami N., Chiumenti M., Cervera M., Rossi R., Chasco U., Domingo M., *Numerical and experimental analysis of the structural performance of AM components built by fused filament fabrication*, International Journal of Mechanics and Materials in Design, vol. 17, iss. 1, 2020, pp. 225–244, <https://doi.org/10.1007/s10999-020-09524-8>.
- [36] Hart K. R., Wetzel E. D., *Fracture behavior of additively manufactured acrylonitrile butadiene styrene (ABS) materials*,

- Engineering Fracture Mechanics, vol. 177, 2017, pp. 1–13, <https://doi.org/10.1016/j.engfracmech.2017.03.028>.
- [37] **Sharafi S., Santare M. H., Gerdes J., Advani S. G.**, *A review of factors that influence the fracture toughness of extrusion-based additively manufactured polymer and polymer composites*, Additive Manufacturing, vol. 38, 2021, p. 101830, <https://doi.org/10.1016/j.addma.2020.101830>.
- [38] **Conway K. M., Pataky G. J.**, *Crazing in additively manufactured acrylonitrile butadiene styrene*, Engineering Fracture Mechanics, vol. 211, 2019, pp. 114–124, <https://doi.org/10.1016/j.engfracmech.2019.02.020>.
- [39] **Parast M. S. A., Bagheri A., Kami A., Azadi M., Asghari V.**, *Bending fatigue behavior of fused filament fabrication 3D-printed ABS and PLA joints with rotary friction welding*, Progress in Additive Manufacturing, 2022, pp. 1–17, <https://doi.org/10.1007/s40964-022-00307-5>.
- [40] **Ziemian C. W., Ziemian R. D., Haile K. V.**, *Characterization of stiffness degradation caused by fatigue damage of additive manufactured parts*, Mater Design, vol. 109, 2016, pp. 209–218, <https://doi.org/10.1016/j.matdes.2016.07.080>.
- [41] **Truss R. W., Chadwick G. A.**, *Tensile deformation behaviour of ABS polymers*, Journal of Materials Science, vol. 11, iss. 1, 1976, pp. 111–117, <https://doi.org/10.1007/BF00541081>.
- [42] **Conway K. M., Kunka C., White B. C., Pataky G. J., Boyce B. L.**, *Increasing fracture toughness via architected porosity*, Journal of Materials Science, vol. 205, 2021, p. 109696, <https://doi.org/10.1016/j.matdes.2021.109696>.
- [43] **ASTM D790-10**, *Standard test methods for flexural properties of unreinforced and reinforced plastics and electrical insulating materials*, ASTM International, West Conshohocken, PA, 2010.
- [44] *** **Stratasys, Ltd.**, *ABSplus-P430 Production-grade thermoplastic for 3D printers*, 2020 [cited 7 April 2022], Available from :http://www.stratasys.com/-/media/files/material-spec-sheets/mss_fdm_absplusp430_1117a.pdf
- [45]*** **ISO/ASTM 52921-2013(E)**, *Standard terminology for additive manufacturing - Coordinate systems and test methodologies*, ASTM International, West Conshohocken, PA, 2013, p. 14.
- [46] **Lluch-Cerezo J., Meseguer M. D., García-Manrique J. A., Benavente R.**, *Influence of Thermal Annealing Temperatures on Powder Mould Effectiveness to Avoid Deformations in ABS and PLA 3D-Printed Parts*, Polymers, vol. 14, iss. 13, 2022, p. 2607, <https://doi.org/10.3390/polym14132607>.
- [47] **Zharylkassyn B., Perveen A., Talamona D.**, *Effect of process parameters and materials on the dimensional accuracy of FDM parts*, Materials Today: Proceedings, vol. 44, iss. 1, 2021, pp. 1307–1311, <https://doi.org/10.1016/j.matpr.2020.11.332>.
- [48] **Camposeco-Negrete C.**, *Optimization of FDM parameters for improving part quality, productivity and sustainability of the process using Taguchi methodology and desirability approach*, Progress in Additive Manufacturing, vol. 5, iss. 1, 2020, pp. 59–65, <https://doi.org/10.1007/s40964-020-00115-9>.
- [49] **Dey A., Yodo N.**, *A systematic survey of FDM process parameter optimization and their influence on part characteristics*, Journal of Manufacturing and Materials Processing, vol. 3, iss. 3, 2019, p. 64, <https://doi.org/10.3390/jmmp3030064>.
- [50] **Yin, B., He, Q., Ye, L.**, *Effects of deposition speed and extrusion temperature on fusion between filaments in single-layer polymer films printed with FFF*, Advanced Industrial and Engineering Polymer Research, vol. 4, iss. 4, 2021, pp. 270–276, <https://doi.org/10.1016/j.aiepr.2021.07.002>.
- [51] **Nabavi-Kivi A., Ayatollahi M. R., Rezaeian P., Razavi S. M. J.**, *Investigating the effect of printing speed and mode mixity on the fracture behavior of FDM-ABS specimens*, Theoretical and Applied Fracture Mechanics, vol. 118, 2022, p. 103223, <https://doi.org/10.1016/j.tafmec.2021.103223>.
- [52] **Quinn G. D., Sparenberg B. T., Koshy P., Ives L. K., Jahanmir S., Arola D. D.**, *Flexural strength of ceramic and glass rods*, J Testing Evaluation, vol. 37, iss. 3, 2009, pp. 222–244.

APPENDIX A

The dimension and density of the AM-FFF ABS specimens were measured and calculated. The schematic drawings of the calculated bending moment, as well as the CS of the three-point bend test specimen, including the l , h and b dimensions, are shown in Fig. A1.

Transmitted-light fractography (TLF) methodology (Fig. A2, five steps flowchart) was developed to examine the AM-FFF ABS specimens' surface and to observe the surrounding area of the crack path. For this method, light is transmitted from a light illuminator through the transparent or translucent specimen to the viewing lens. This method may assist in determining the crack propagation path

of specimens such as the AM-FFF ABS specimens (Fig. A3).

A universal MTS testing machine was used to test the mechanical properties, equipped with a three-point bending fixture and a deflection gage. The bending test presents two parameters: (1) axial deflection and (2) force in Newtons. The deflection vs. load curves were obtained by the AM-FFF ABS specimens three-point bend tests for the six configurations: flat $0^\circ/90^\circ$, flat $-45^\circ/+45^\circ$, on-edge $0^\circ/90^\circ$, on-edge $-45^\circ/+45^\circ$, upright $0^\circ/90^\circ$ and upright $-45^\circ/+45^\circ$ (Fig. A3). The mechanical properties of the AM-FFF ABS three-point bending experimental results for the six examined configurations are summarized in Tables A1-A6.

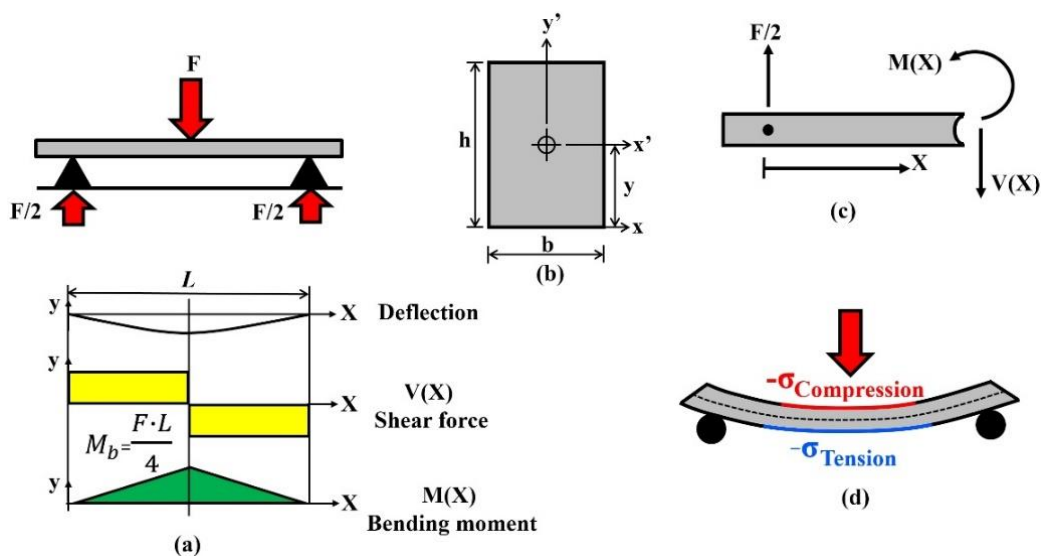


Fig. A1. The three-point bend test specimen: (a) schematic drawing of the calculated bending moment; (b) the cross-section (CS) of the three-point bend specimen; (c) the specimen's moment of inertia; and (d) the bent specimen, showing the compression and tension stresses.

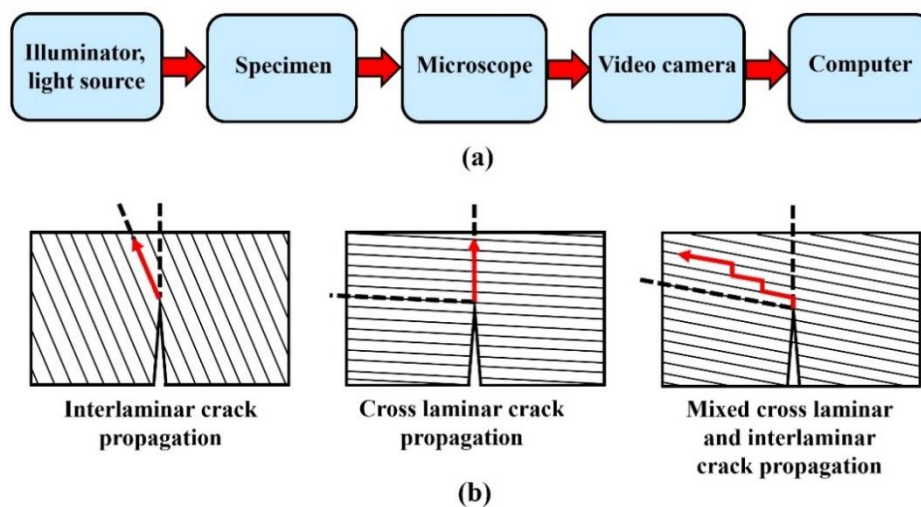


Fig. A2. Transmitted-light fractography (TLF) for examination of the specimens' surface and for observation of the vicinity of the crack path: (a) schematic illustration of the TLF process; and (b) illustration of the different crack propagation paths of the AM-FFF ABS specimens

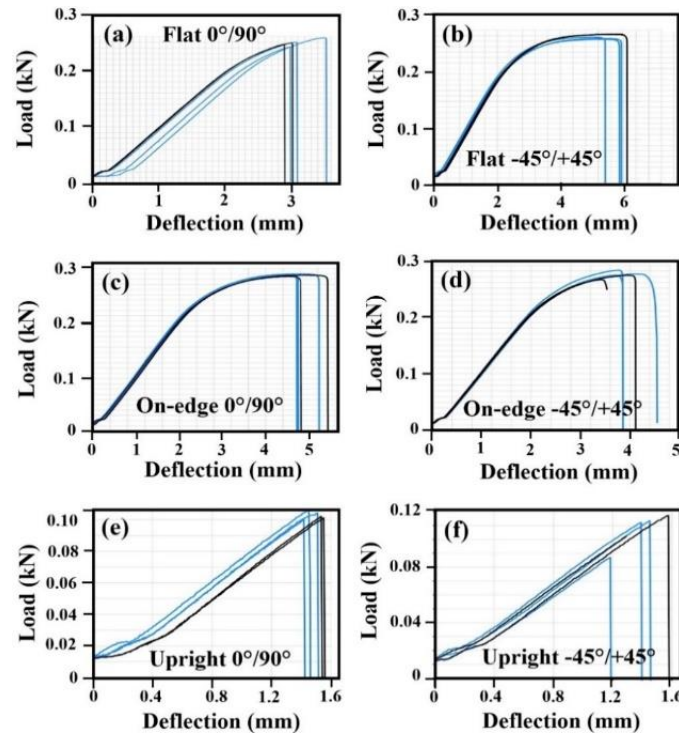


Fig. A3. Experimental results of the load vs. deflection for the six tested configuration: (a) flat $0^\circ/90^\circ$ specimen; (b) flat $-45^\circ/+45^\circ$ specimen; (c) on-edge $0^\circ/90^\circ$ specimen; (d) on-edge $-45^\circ/+45^\circ$ specimen; (e) upright $0^\circ/90^\circ$ specimen; and (f) upright $45^\circ/+45^\circ$ specimen

Table A1. Properties of the flat (F) $0^\circ/90^\circ$ configuration of the AM-FFF ABS three-point bending experimental results, where ρ_{AM-FFF} is the AM-FFF specimens' relative density, δ is the deflection and σ is the flexural strength. S.D. represents the standard deviation

Specimen configuration	ρ_{AM-FFF} (%)	δ (mm)	σ (MPa)
1 F $0^\circ/90^\circ$	96.5	3.5	61.3
2 F $0^\circ/90^\circ$	96.0	3.5	57.1
3 F $0^\circ/90^\circ$	94.7	3.1	58.4
4 F $0^\circ/90^\circ$	94.0	3.0	57.3
5 F $0^\circ/90^\circ$	95.2	2.9	57.6
Average \pm S.D.	95.5\pm1.0	3.2\pm0.2	58.3\pm1.5

Table A2. Properties of the Flat (F) $-45^\circ/+45^\circ$ configuration of the AM-FFF ABS three-point bending experimental results, where ρ_{AM-FFF} is the AM-FFF specimens' relative density, δ is the deflection and σ is the flexural strength. S.D. represents the standard deviation

Specimen configuration	ρ_{AM-FFF} (%)	δ (mm)	σ (MPa)
1 F $-45^\circ/+45^\circ$	94.1	5.1	61.4
2 F $-45^\circ/+45^\circ$	94.4	5.3	61.6
3 F $-45^\circ/+45^\circ$	94.7	5.0	62.5
4 F $-45^\circ/+45^\circ$	95.7	5.4	63.9
5 F $-45^\circ/+45^\circ$	96.2	5.8	64.6
Average \pm S.D.	95.3\pm1.0	5.4\pm0.3	62.8\pm1.3

Table A3. Properties of the on-edge (OE) $0^\circ/90^\circ$ configuration of the AM-FFF ABS three-point bending experimental results, where ρ_{AM-FFF} is the AM-FFF specimens' relative density, δ is the deflection and σ is the flexural strength. S.D. represents the standard deviation

Specimen configuration	ρ_{AM-FFF} (%)	δ (mm)	σ (MPa)
1 OE $0^\circ/90^\circ$	97.6	4.6	70.3
2 OE $0^\circ/90^\circ$	96.8	4.8	70.6

Specimen configuration	ρ_{AM-FFF} (%)	δ (mm)	σ (MPa)
3 OE0°/90°	99.4	4.5	72.9
4 OE0°/90°	96.9	4.5	69.5
5 OE0°/90°	97.4	5.0	70.6
6 OE0°/90°	96.3	5.3	71.7
7 OE0°/90°	95.2	5.3	69.6
8 OE0°/90°	96.6	4.4	69.9
9 OE0°/90°	95.4	5.5	70.7
10 OE0°/90°	95.7	4.9	70.0
11 OE0°/90°	94.3	4.9	68.8
Average \pm S.D.	96.8\pm1.3	4.9\pm0.4	70.4\pm1.1

Table A4. Properties of the on-edge (OE) -45°/+45° configuration of the AM-FFF ABS three-point bending experimental results, where ρ_{AM-FFF} is the AM-FFF specimens' relative density, δ is the deflection and σ is the flexural strength. S.D. represents the standard deviation

Specimen configuration	ρ_{AM-FFF} (%)	δ (mm)	σ (MPa)
1 OE-45°/+45°	98.2	4.1	65.1
2 OE-45°/+45°	97.8	3.7	64.5
3 OE-45°/+45°	98.4	3.8	66.5
4 OE-45°/+45°	98.3	3.9	64.3
5 OE-45°/+45°	97.4	3.4	62.3
6 OE-45°/+45°	94.4	5.8	63.9
7 OE-45°/+45°	95.3	7.2	69.4
8 OE-45°/+45°	95.9	4.5	65.5
9 OE-45°/+45°	93.1	6.5	64.9
10 OE-45°/+45°	94.2	6.1	66.5
11 OE-45°/+45°	94.3	5.7	66.2
Average \pm S.D.	96.3\pm1.9	5.0\pm1.26	65.4\pm1.8

Table A5. Properties of the upright (UR) 0°/90° configuration of the AM-FFF ABS three-point bending experimental results, where ρ_{AM-FFF} is the AM-FFF specimens' relative density, δ is the deflection and σ is the flexural strength. S.D. represents the standard deviation

Specimen configuration	ρ_{AM-FFF} (%)	δ (mm)	σ (MPa)
1 UR 0°/90°	91.4	1.4	23.6
2 UR 0°/90°	90.7	1.5	24.3
3 UR 0°/90°	90.8	1.4	25.2
4 UR 0°/90°	92.2	1.6	24.1
5 UR 0°/90°	90.6	1.5	23.8
Average \pm S.D.	91.1\pm0.6	1.5\pm0.1	24.2\pm0.6

Table A6. Properties of the upright (UR) -45°/+45° configuration of the AM-FFF ABS three-point bending experimental results, where ρ_{AM-FFF} is the AM-FFF specimens' relative density, δ is the deflection and σ is the flexural strength. S.D. represents the standard deviation

Specimen configuration	ρ_{AM-FFF} (%)	δ (mm)	σ (MPa)
1 UR-45°/+45°	92.3	1.5	26.7
2 UR-45°/+45°	90.5	1.2	20.2
3 UR-45°/+45°	91.9	1.4	26.4
4 UR-45°/+45°	91.2	1.3	24.0
5 UR-45°/+45°	89.1	1.6	26.7
Average \pm S.D.	91.1\pm1.0	1.4\pm0.1	24.8\pm2.5